Ambient-Noise Wave-Equation Tomography of the Alps and Ligurian-Provence Basin

Ahmed Nouibat, Romain Brossier, Laurent Stehly, Jian Cao, Anne Paul

Ambient-Noise Wave-Equation Tomography of the Alps and Ligurian-Provence Basin

A. Nouibat[1], R. Brossier[1], L. Stehly[1], J. Cao[1], A. Paul[1], Cifalps Team, and AlpArray Working Group[2]

[1]Univ. Grenoble Alpes, Univ. Savoie Mont Blanc, CNRS, IRD, UGE, ISTerre, *38000 Grenoble, France*

[2]See Appendix A

Key Points:

- A new 3-D velocity model of the crust and upper mantle beneath the Alps and Northwestern Mediterranean, based on wave-equation tomography
- 3-D acoustic-elastic waveform modeling of Rayleigh-Scholte waves from ambient noise
- 3-D high-resolution Moho depth map of the Alps and Ligurian-Provence basin

Corresponding author: A. Nouibat, ahmed.nouibat@univ-grenoble-alpes.fr

Abstract

Taking benefit of the AlpArray temporary network and permanent networks in W-Europe, we construct a 3-D onshore-offshore velocity model of the crust and upper mantle using ambient-noise wave-equation tomography (WET). We use a frequency-dependent phase traveltime misfit function in an iterative procedure to refine a recent 3-D V_s model computed from a Bayesian two-step ambient noise tomography (ANT). Observed waveforms consist in vertical-component noise correlations from 600 broadband stations in the Alps and surroundings, including ocean-bottom seismometers (OBS) in the Ligurian sea. We perform 3-D inversion in the 5-85 s period range. In the long-period band (20-85 s), an elastic approximation is considered, while in the 5-20 s band, we account for the effect of water layer in the Ligurian sea by applying a fluid-solid coupling for acoustic-elastic waveform simulations. The resulting V_s model enhances the shape and contrast of velocity structures, accounting for 3-D and finite-frequency effects. It emphasizes the deep sediments of the Ligurian-Provence basin and focuses the low-velocity anomalies of the crust in the W-Alps. We obtain a high-resolution Moho depth map covering the Alps and Ligurian sea. In the W-Alps, this map confirms the deepening of the European crust following the subduction beneath Adria and the existence of major structures such as the Moho jump beneath the external crystalline massifs and shallow depths associated with the Ivrea Body. It provides further constraints on the deep structure beneath the Ligurian-Provence basin, regarding the lateral and along-strike crustal-thickness variations from the oceanic domain to the conjugate margins.

Plain Language Summary

In the complex tectonic setting of the Alps and Northwestern Mediterranean, a precise seismic mapping of the 3-D structure of Moho is crucial to understand the deep dynamic processes involved in the orogenesis of the western Alps and the opening of the Ligurian-Provence back-arc basin. Using an innovative wave-equation tomography (WET) of ambient noise recordings, we compute a high-resolution velocity model covering the Alps and Ligurian sea. In particular, we account for the influence of water and seabed relief on the 3-D propagation of surface waves in the Ligurian sea. We derive a high-resolution onshore-offshore 3-D map of Moho depth beneath the Alps and Ligurian-Provence basin. Our Moho map confirms the subduction of the European lithosphere beneath Adria. It shows strong

depth variations in the Ligurian-Provence basin, from 12 km in the basin axis to $\sim$ 20-25 km in the conjugate margins of Provence and Corsica.

1 Introduction

The geodynamic evolution in the Alps and Northwestern Mediterranean occurs in a context of plate reorganization, dominated since the Late Cretaceous by the convergence between the European and African plates (e.g., Schmid et al., 2004; Faccenna et al., 2014). In this convergence context, the western Alps result from three successive tectonic episodes involving Europe, the Adria micro-plate and the Tethyan oceanic domain (Tethys) in between: (i) closure of the oceanic domain by subduction from Late Cretaceous to Early Eocene (e.g., Handy et al., 2010); (ii) continental subduction of the European margin beneath Adria during the Late Eocene (e.g., Chopin, 1984; Duchêne et al., 1997; Guillot et al., 2009; Zhao et al., 2015); (iii) continental collision from Oligocene onwards (e.g., Polino et al., 1990; Dumont et al., 2012). This multiphase evolution led to a complex present-day arcuate architecture of Western Alps, where different units are involved (Fig. 1): (i) to the west, the European continental domain (or European foreland) corresponding to the lower plate; (ii) to the east, the Adria continental domain (or Adriatic foreland) corresponding to the upper plate; (iii) the Eocene subduction wedge (or accretionary prism) in between, bounded by two major crustal-scale faults: the Frontal Pennine Fault (PFT) to the west and the dextral strike-slip Insubric Fault (IF) to the east. During Miocene and Pliocene Epochs, the opening of back-arc extensional basins occurred at the back of the Adria northwest-dipping subduction zone (e.g., Gueguen et al., 1998; Jolivet et al., 2020). This extension started along the Provence region leading to the Ligurian-Provence basin, and has further spread from east to west and south, resulting in the opening of the Algerian basin, and later, of the Tyrrhenian basin (e.g., Rollet et al., 2002; Séranne, 1999). The opening of the Ligurian-Provence basin initiated at 35 Ma by a rifting phase between Europe and the Corsica-Sardinia block. The progressive south-eastward roll-back and retreat of the Adria slab below the Corsica-Sardinia domain led to Oligocene stretching of the continental crust followed by continental break-up during the early Miocene, and to the genesis of an oceanic crust between 15 and 11 Ma (e.g., Séranne, 1999; Jolivet & Faccenna, 2000). As a result, three principal domains, mainly identified from active seismic data, describe the present-day geological setting of the Ligurian-Provence basin (Fig. 1): (i) two thinned conjugate continental passive margins corresponding to the Ligurian-Provence margin to the north and

Corsican margin to the south; (ii) an oceanic domain in between, described as an 'atypical oceanic crust' by Rollet et al. (2002) because it is thinner than normal oceanic crust; (iii) two transitional domains separating the margins and the oceanic domain, likely made up of a very thin continental crust overlying a thick rift-related corner of magmatic underplating (e.g., Séranne, 1999).

The complex geodynamic context associated with the interaction between the opposing vergence subductions of Europe and the Apennines has resulted in a three-dimensional, heterogeneous lithospheric structure that is difficult to image by seismology. Consequently, questions remain regarding the role of the 3-D geometry of European continental subduction in the present-day architecture of Western Alps (e.g., Malusà et al., 2021), and the role of the rapid retreat of Apennines subduction in the present-day petrological-lithological composition of the crust beneath the Ligurian-Provence basin (e.g., Rollet et al., 2002). Thus, accurate 3-D seismic imaging of the crust and upper mantle is critically needed to complement the 2-D seismological observations, especially since the region benefits from a fairly wide coverage of seismological stations, including the newly deployed AlpArray land-sea network (AASN, Hetényi et al., 2018).

With the deployment of the AlpArray temporary seismic network, Western Europe has become one of the most densely instrumented areas in the world. More specifically, the region consisting of the Alps and the Ligurian sea includes, in addition to the onshore part of AlpArray, other temporary experiments such as Cifalps-2 in the northwestern Alps (Zhao et al., 2018) and the marine part of AlpArray in the Ligurian-Provence basin. These dense and high-quality surveys provide an ideal set up to use seismic ambient noise records to resolve the crust and upper mantle, as well as major interfaces such as the Moho. Several ambient noise tomography (ANT) were conducted in the region. Following on from the large-scale ANT by Lu et al. (2018), which used a part of the land component of AlpArray, the recent ANT by Nouibat et al. (2022a, 2022b) was the first study to use the entire AlpArray network, resulting in a land-sea model covering the Alps and Northwestern Mediterranean. These large-scale models, and other models focusing on specific regions such as the western Alps (Kästle et al., 2018; Zhao et al., 2015, 2020), the southeastern Alps (Sadeghi-Bagherabadi et al., 2021), the Vienna basin (Schippkus et al., 2020), the Bohemian massif (Kvapil et al., 2021), the Ligurian sea, (Wolf et al., 2021; Magrini et al., 2022), have substantially improved existing knowledge and have provided new insights into the complex deep structure of the region. They highlighted Moho jumps beneath the external crystalline massifs (Lu

et al., 2018; Nouibat et al., 2022a) and Moho dipping following the subduction of European continental crust in the southern Western Alps (Zhao et al., 2015, 2020; Nouibat et al., 2022a), and provided clues about the lithological nature of the crust in the Ligurian basin (Wolf et al., 2021; Nouibat et al., 2022b).

The above-mentioned models have been derived using conventional ANT, which involves two steps: (1) 2-D traveltime inversion for group or phase velocity maps, and (2) 1-D depth inversion for V_s based on local dispersion curves. This procedure has two limitations that may bias the geological interpretations: (1) the ray theory assumption when computing 2-D Rayleigh-wave velocity maps, which is only valid in the high-frequency case (e.g., Snieder, 1986; Cerveny, 2003), and (2) the local 1-D nature of the depth inversion in the second step, which does not account for the 3-D lateral heterogeneity of the medium, thus limiting the velocity model to be pseudo-3-D by construction. The aim of our study is to overcome these limitations in the context of Western Alps and Ligurian-Provence basin by building a self-consistent onshore-offshore 3-D velocity model using a wave-equation tomography of ambient noise. This allows us to take into account the effect of 3-D structures and of the water layer in the Ligurian sea on the propagation of surface waves. Indeed, wave-equation-based tomographic methods are an alternative of choice to overcome such assumptions, as they naturally accommodate for 3-D heterogeneity and finite-frequency effects, thus providing more realistic sensitivity kernel for surface waves. These approaches consist in iteratively updating the velocity model by minimising a misfit function between observed and synthetic waveforms obtained through 3-D numerical modeling of seismic wave propagation.

In the following, we refer to ANT when the two-step method is used to invert the correlations, to FWI when the seismic wave propagation is modeled in 3-D by solving the wave equation and the misfit function involves the waveform i.e. phase and amplitude (e.g., Virieux & Operto, 2009, and references herein), and to wave equation tomography (WET) when the misfit function involves only the phase (e.g., Luo & Schuster, 1991; Tape et al., 2010).

With the availability of accurate large-scale seismic wavefield modeling and computing resources, wave-equation-based tomographic methods have been widely applied to the crust and upper mantle (e.g., Tape et al., 2010; H. Zhu et al., 2012; Yuan et al., 2014; Fichtner & Villaseñor, 2015; Beller et al., 2018), often providing higher resolution images than those obtained from ray theory and finite-frequency tomography. However, their application to

ambient noise data is challenging. Indeed, noise correlations provide the Green's function of the medium only under certain conditions, for instance when considering a homogeneous distribution of uncorrelated noise sources (Wapenaar, 2004; Roux et al., 2005), or more generally assuming equipartition of the noise wavefield (Lobkis & Weaver, 2001; Snieder et al., 2007; Weaver & Lobkis, 2001; Campillo, 2006). These conditions are rarely fully met in practice. There are two ways to deal with this difficulty.

The first way consists in taking into account the distribution of the noise sources when computing synthetic noise correlations and their sensitivity kernels. Indeed, the cross-correlations waveforms can be strongly affected by the distribution of noise sources (Tromp et al., 2010; Fichtner, 2014) and by the processing applied to the noise records (Bensen et al., 2007; Fichtner et al., 2016, 2020). In particular, the amplitude of noise correlations depends mostly on the energy and distribution of the noise sources (e.g., Hanasoge, 2014). As a consequence, spatial variations of noise correlation amplitude cannot be interpreted unambiguously as lateral contrasts of attenuation (Tsai, 2011; Stehly & Boué, 2017) but can be used to image the distribution of noise sources (Stehly & Boué, 2017; Ermert et al., 2016, 2017, 2021; Igel et al., 2021, 2023). Therefore, methodological efforts have been done to apply FWI to noise correlations without assuming that they are similar to the Green's function of the medium, but by treating them as self-consistent observables. This requires to jointly invert for the distribution of noise sources and the Earth structure in order to take into account the distribution of noise sources when computing synthetic noise correlations and their sensitivity kernels (Tromp et al., 2010; Fichtner, 2014; Sager et al., 2018a, 2018b; Hanasoge, 2014). However applying this approach to image the crust and upper mantle at a continental scale remains challenging due to the complexity of the dynamics of microseismic noise sources and the heterogeneity of the medium.

An alternative approach is to apply wave equation tomography (Luo & Schuster, 1991) rather than FWI to noise correlations. Indeed, while heterogeneous distribution of noise sources and data processing affect the correlations waveforms, traveltime measurements of the correlations surface-wave fundamental mode are less affected (Tsai, 2009; Froment et al., 2010; Tsai, 2011; Fichtner, 2014; Delaney et al., 2017). Consequently, in crustal environment, the traveltime residuals depend more on the heterogeneity of the medium than on the source distribution (Yang & Ritzwoller, 2008; Froment et al., 2010; Kimman & Trampert, 2010). It is thus possible to assume that at least a subset of the correlations provide accurately the Green's function surface-wave dispersion. Hence to apply WET, noise

correlations are modeled assuming that they are similar to the Green's function, i.e. without taking into account the distribution of noise sources. In this case the traveltime (phase) of surface-wave fundamental mode is inverted rather than the waveform. However, this approach has two main limitations: (1) it does not account for the noise sources distribution which can bias the apparent arrival time of surface waves (Tsai, 2009; Froment et al., 2010; Delaney et al., 2017). This is mitigated in practice by selecting only station pairs for which the arrival time of surface waves is similar in the positive and negative correlation time; (2) noise correlations that contain mostly the fundamental mode of surface waves are compared with synthetic correlations that contains all possible mode of propagation. This may affect misfit measurements if the different modes are not well separated in time. Nevertheless, WET applications to noise correlations has recently demonstrated its potential to provide accurate velocity models of the crust and upper mantle that better explain the observations than conventional ANT (Chen et al., 2014; Liu et al., 2017; Lu et al., 2020).

Using the ANT model from Lu et al. (2018) as an initial model, Lu et al. (2020) were the first to apply wave-equation tomography to the alpine region using noise correlations. They demonstrated that WET is relevant to obtain models that better explain the data, and to improve the resolution of ANT models in the Alps. However, their WET model does not cover the Ligurian sea since the offshore part of the AlpArray network was not yet available. We refer the reader to Nouibat et al. (2022a, 2022b) for more details about the comparison of recent ANT methodologies and models in the region.

In this study, we improve the WET methodology used by Lu et al. (2020). Theses improvements consist in: (i) performing an acoustic-elastic coupled wave-equation tomography to better represent the wave-physics and consider more realistic constraints on velocity structure in the oceanic domain of the Ligurian basin and along the continental margins; (ii) inverting seismic data in a broader band (5-85 s) in order to constrain the shallow part of the crust as well as the upper mantle, employing a hierarchical inversion strategy that avoids possible cycle-skipping issues; (iii) using a random sub-sampling scheme over 185 virtual sources rather than a fixed number of virtual sources. Similar to Lu et al. (2020), we minimize the frequency-dependent phase traveltime differences of Rayleigh waves and tackle the inversion using the SEISCOPE SEM46 code originally developed for exploration scales (Trinh et al., 2019). Taking advantage of the densest seismological coverage in Western Europe including the entire AlpArray network, we perform a large-scale wave-equation

tomography in order to refine the land-sea model by Nouibat et al. (2022a) obtained from conventional ANT.

The availability of Rayleigh-wave traveltime measurements across and within the Ligurian sea, and the latest developments of full waveform modeling and inversion in the fluid-solid coupled media (Cao et al., 2022), motivated us to go further in the improvement of wave-equation tomography by considering the effect of the water layer on the 3-D propagation of surface waves from ambient noise correlations.

In an oceanic domain, two different types of surface waves can be recorded on the vertical component. At large periods, when the wavelength of the surface waves is large compared to the thickness of the water layer, the effect of the water on wave propagation is negligible, and the surface waves propagate as Rayleigh waves. At shorter periods, however, the effect of the water layer can no longer be neglected and the surface wave propagates as a Rayleigh-Scholte wave, which is a fluid-solid interface wave. Nouibat et al. (2022b) have shown that a water layer thicker than 0.5 km can have a significant effect on the Rayleigh-Scholte wave dispersion at period $\leq 20\ s$ and should therefore be taken into account in tomographic studies. Thus, several studies have taken the water column into account when inverting the local dispersion curve of Ralyeigh-Scholte waves extracted from noise correlation into a local 1-D V_s model (e.g., Mordret et al., 2014; Guerin et al., 2020; Wolf et al., 2021; Nouibat et al., 2022b; Carvalho et al., 2022). However, this assumes a strictly 1-D coupling in a laterally homogeneous medium.

In our study, the 3-D effects of the presence of water layer are considered on the surface-wave propagation. For this purpose, we apply the technique of acoustic-elastic coupling in the waveform modeling to deal with the seabed relief. The objective is twofold. Firstly, to investigate the influence of the water layer on the propagation of surface waves between onshore and sea-bottom stations, more specifically Rayleigh-Scholte waves. To our knowledge, this is the first study documenting the influence of the water layer on the 3-D propagation of ambient noise surface waves. Secondly, to incorporate the fluid-solid coupling in the inversion framework, which makes this study the first ambient noise wave-equation tomography to take into account the effect of the water layer.

The structure of the manuscript is organized as follows. Section 2 describes the dataset of ambient noise correlations and the initial velocity model used in the wave-equation tomography. The overall methodology is presented in Sections 3–4. Section 3 introduces the

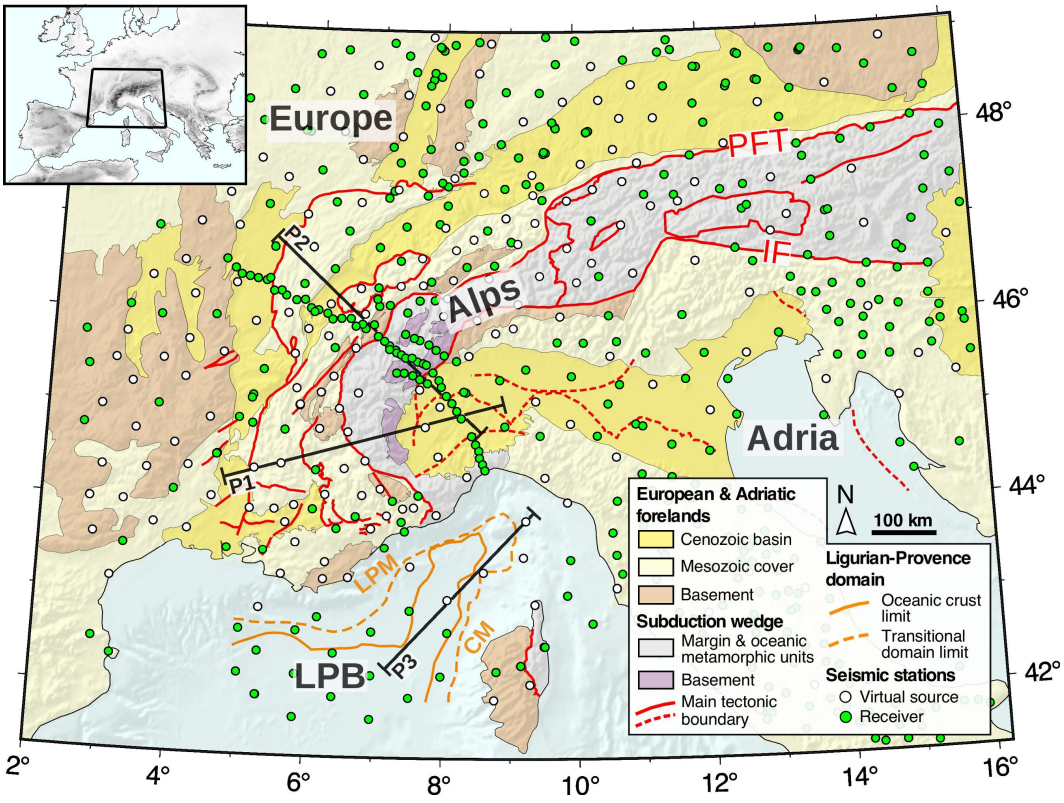

Figure 1. Geological and tectonic setting of the study area, modified from Handy et al. (2010) and Rollet et al. (2002), with locations of seismic stations used in this work (white circles: virtual sources; green circles: receivers). LPB: Ligurian-Provence basin, LPM: Ligurian-Provence margin, CM: Corsican margin. Black lines show locations of the seismic profiles discussed in the text.

iterative process of the WET workflow, while Section 4 is dedicated to 3-D modeling of surface waves, with emphasis on the acoustic-elastic case. In the light of the specific case of the Ligurian-Provence basin, we document the importance of the fluid-solid coupling for marine crustal imaging based on ambient noise data. Section 5 presents tomography results and related discussions. In Section 6, we assess the robustness of the resulting 3-D velocity model.

2 Data

2.1 Ambient Noise Data

We use a subset of the data used by Nouibat et al. (2022a, 2022b) consisting of vertical component cross-correlations computed between 600 broadband stations from all available temporary and permanent networks in the Alpine region (Fig. 1, 2°E-16.2°E; 41.3°N-49.1°N)

during the period 2015-2019. The station array includes the entire AlpArray Seismic Network (AASN) and the Cifalps-2 experiment.

The offshore component of the dataset consists of high-quality correlations between the AASN OBSs obtained from an iterative procedure involving onshore stations of the AASN and permanent networks. Beforehand, the OBSs daily noise records were cleaned from transients (e.g., glitches) and seafloor-induced noises (compliance, tilt). For more details about this specific processing, readers can refer to Nouibat et al. (2022b).

We keep only reliable cross-correlations by applying the following criteria: (1) signal-to-noise ratio (SNR) greater than 5, (2) difference in group velocity measured on the positive and negative parts less than 0.2 km/s, and (3) inter-station distance larger than one wavelength for the maximum period considered in each period band. The SNR is defined as the ratio of the maximum amplitude of the surface wave to the standard deviation of the signal starting after the surface wave window. The final dataset includes $\sim 22 \times 10^3$ to 55×10^3 high-quality cross-correlations depending on the period band (Table. 1). For the wave-equation tomography, all stations in Figure 1 serve as receivers, out of which 185 stations are used as virtual sources (white circles).

2.2 Initial Model

The initial model consists of the 3-D onshore-offshore V_s model by Nouibat et al. (2022a, 2022b), and a V_p model converted from this V_s by the empirical formula from Brocher (2005): $V_p = 0.9409 + 2.0947V_s - 0.8206V_s^2 + 0.2683V_s^3 - 0.0251V_s^4$. The V_s model by Nouibat et al. (2022a, 2022b) was obtained from ambient noise tomography using all available permanent and temporary seismic networks in Western Europe from 2015 to 2019. This model is derived from a hybrid data-driven tomography involving a 2-D transdimensional Bayesian inversion for group-velocity maps and their uncertainties, and a 1-D probabilistic inversion for V_s at depth. The onshore part of this model has been validated in the western Alps by comparison with other available geophysical studies, e.g, receiver functions (RFs), controlled-source seismic (CSS) experiments, Bouguer anomaly, along the Cifalps-1 & Cifalps-2 profiles (Nouibat et al., 2022a; Paul et al., 2022). The offshore part has been validated by comparison with a high-resolution V_p cross-section derived from refraction and wide-angle seismic profiling along the axis of the Ligurian basin (Nouibat et al., 2022b). However, it remains limited by the assumptions made in the two steps of the inversion, in particular the high-frequency

assumption for Rayleigh-wave propagation in the 2-D inversion, and the 1-D assumption in the inversion for V_s. Because of the 1-D assumption, they assumed a 1-D fluid-solid coupling in the oceanic domain, which is not suitable for dispersion of Rayleigh-Scholte waves or conversion of Rayleigh waves to Rayleigh-Scholte waves across the margins. The objective of the present study is to overcome these limitations and improve the resolution of the V_s model by performing 3-D wave-equation tomography.

3 Iterative Inversion Scheme

Similar to Lu et al. (2020), we formulate the inverse problem as the minimization of the misfit function (ξ) defined by the differences of frequency-dependent phase traveltime between observed and synthetic vertical-component waveforms of ambient-noise Rayleigh waves

$$\underset{\mathbf{m}}{\operatorname{argmin}}\, \xi(\mathbf{m}) = \frac{1}{2} \sum_i \sum_\omega \Delta T_i(\omega, \mathbf{m})^2, \tag{1}$$

where $\Delta T_i(\omega, \mathbf{m})$ is the phase traveltime residual for the ith station pair at frequency ω, given the model parameters ($\mathbf{m}$). We measure ΔT using a multi-taper technique (Tape et al., 2010). We tackle the minimization of (ξ) using a quasi-Newton local optimization method, with the following iterative scheme (Métivier & Brossier, 2016):

$$\mathbf{m}_{k+1} = \mathbf{m}_k + \alpha_k \delta \mathbf{m}_k \tag{2}$$

where α_k is the step length estimated by line search strategy and $\delta \mathbf{m}_k = -B_k \nabla \xi(\mathbf{m}_k)$ is the model update in which B_k is an approximation of the inverse of the Hessian matrix (i.e. the second-order derivative of ξ with respect to model parameters). We use the limited memory version of quasi-Newton methods (l-BFGS, Nocedal, 1980) to estimate B_k using gradients at few previous iterations. We update the velocity model by inverting from low to high frequencies, in four narrow period bands: 5-10 s, 10-20 s, 20-40 s, and 40-85 s. Given the dispersive character and depth sensitivity of the Rayleigh-wave phase velocity at these periods, such a hierarchical approach is useful to prevent cycle skipping issue. This approach first constrains large-scale anomalies in the upper mantle part of the model using the long-period content, then it constrains small-scale anomalies in its crustal part using the short-period content.

We reconstruct simultaneously V_s and V_p to account for the sensitivity of the Rayleigh-wave to V_p, which becomes non-negligible at short periods (e.g., Eddy & Ekström, 2014; Qiao et al., 2018). Therefore, the relative perturbation of the misfit function (ξ) to per-

turbations of the two parameters is given by the linear relation: $\delta\xi(\mathbf{m}) = K_{V_s}(\mathbf{m})\delta \ln V_s + K_{V_p}(\mathbf{m})\delta \ln V_p$, where K_{V_s} and K_{V_p} are the sensitivity kernels for V_s and V_p respectively (i.e. misfit gradients with respect to V_s and V_p). Due to the computational cost of modeling for multiple sources, we employ a randomized sub-sampling strategy of the ensemble of virtual sources over iterations in order to achieve optimal path coverage without compromising the quality of the inversion results, as usually applied for exploration scales (Warner et al., 2013). Following the workflow shown in Fig. 2, our wave-equation-based tomography is summarized in the main steps bellow:

(1) Perform the forward modeling for one subset of 64 virtual sources.

(2) Measure phase traveltime misfits between observed and simulated waveforms and compute the adjoint sources.

(3) Perform the adjoint modeling and extract gradients from cross-correlations of incident and adjoint fields.

(4) Gradients are summed and smoothed using a non-stationary Laplace smoothing filter (approximated by a 2nd-order Bessel filter) to remove high wavenumber artefacts and constrain the inversion (Trinh et al., 2017). The filter is defined by coherent lengths that are directly computed from the inverted parameters V_p and V_s: $L_z = L_x = L_y = 0.1 \times \lambda_l$ where λ_l is the local wavelength at the maximum frequency considered.

(5) Estimate the step length and update the current velocity model.

(6) Change the subset each 3 iterations. The output model after 9 iterations is used as a starting model for the next shorter period band following the same iterative procedure. The density model is updated accordingly using the empirical formula from Brocher (2005): $\rho = 1.6612V_p - 0.4721V_p^2 + 0.0671V_p^3 - 0.0043V_p^4 + 0.000106V_p^5$.

Period band [s]	Nb of elements (nZ,nX,nY)	Element size (dZ, dX, dY) [km]	Nb of data
40 - 85	16, 81, 60	10, 15, 15	31 212
20 - 40	20, 101, 75	8, 12, 12	43 350
10 - 20	27, 152, 112	6, 8, 8	54 870
5 - 10	41, 202, 150	4, 6, 6	22 066

Table 1. Spectral elements number/size and number of measurements used in each period band.

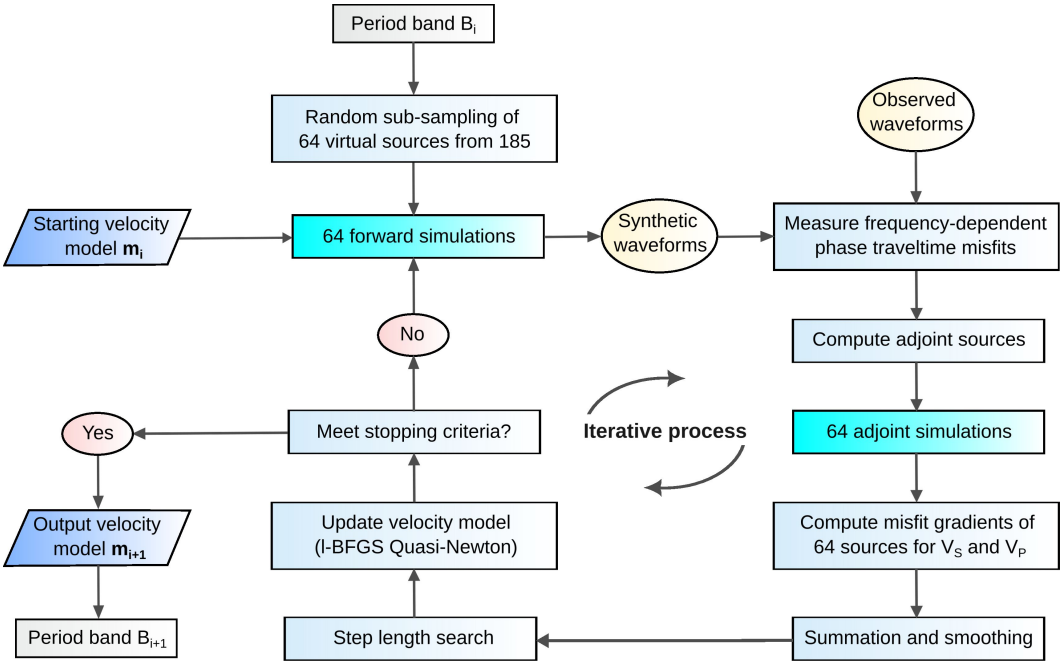

Figure 2. General workflow of the wave-equation tomography (WET).

4 3-D Simulations of Surface-Wave Propagation

We perform forward and adjoint simulations using the time-domain wave equation modeling of the SEM46 spectral-element-based code. We perform simulations for the vertical component of Rayleigh waves by applying a point-force at the location of virtual sources with a filtered Dirac delta as source time function (identical for all virtual sources). Therefore, the synthetic waveform (u_{syn}) at a receiver position for model ($\mathbf{m}$) is the convolution product between the source time function (s) and the synthetic Green's function (G_{syn}) for the source–receiver pair (e.g., Lu et al., 2020): $u_{syn}(\mathbf{m}, t) = s(t) * G_{syn}(\mathbf{m}, t)$. To compare with synthetic waveforms, we convolve the source time function (s) with the time derivative of the noise cross-correlation (C) for the source–receiver pair, which is a good approximation of the Green's function (G) of the target medium (e.g., Lobkis & Weaver, 2001; Snieder, 2004; Wapenaar, 2004; Roux et al., 2005; Weaver, 2005): $u(t) = s(t) * -\partial_t C(t) \approx s(t) * G(t)$. The time sampling of simulation varies from 0.04 to 0.0015 s, with the Courant–Friedrichs–Lewy (CFL) condition satisfied (Komatitsch & Tromp, 1999). Surface waves are extracted in a time window with $min[d/5, t_{max} - 1.5T]$ and $max[d/2, t_{max} + 1.5T]$ as lower and upper limits in the 10-20 s, 20-40 s, and 40-85 s, and a time window with $min[d/4, t_{max} - 2T]$ and $max[d/1.5, t_{max} + 2T]$ as lower and upper limits in the 5-10 s, where d is the inter-station

distance (in km), t_{max} is the arrival time of the maximum of the envelope of synthetic waveform, and T is the maximum period of the considered band.

4.1 Elastic modeling of Rayleigh Waves

We simulate the incident wavefield in the 20-85 s period band by solving the second-order elastic wave equation:

$$\rho_s \partial_{tt} \mathbf{u} = \nabla \cdot \boldsymbol{\sigma} + \mathbf{f}_s, \quad \boldsymbol{\sigma} = \mathbf{C}\boldsymbol{\varepsilon} \tag{3}$$

where $\mathbf{u}$ is the displacement field, $\mathbf{f}_s$ is the force vector, $\boldsymbol{\sigma}$ and $\boldsymbol{\varepsilon}$ are the second-order stress and strain tensors respectively, ρ_s is the solid density and $\mathbf{C}$ is the fourth-order elastic stiffness tensor. We employ a flexible Cartesian-based hexahedral mesh with element size varying from 15 to 6 km in the horizontal direction and from 10 to 4 km in the vertical direction (see Table. 1). The wavefield is interpolated inside each spectral element using Lagrange polynomials of order 4. We parameterize Gauss–Lobatto–Legendre (GLL) points by isotropic S-wave velocity (V_s) starting from the model described in section 2, and (V_p, ρ) computed from V_s (Brocher, 2005). Finally, we vertically deform the mesh grid for an accurate representation of the complex topography(bathymetry) on the free surface and to handle the Earth curvature.

Misfit elementary gradients with respect to the medium parameters are obtained from the zero-lag correlation of adjoint and incident wavefields, based on the adjoint-state method (e.g., Tromp et al., 2005; Plessix, 2006). Adjoint wavefields are obtained by injecting the adjoint sources at receiver locations in the adjoint wave equations. The adjoint source for the multi-taper method is given by the derivative of synthetic waveforms weighted by the frequency-dependent phase difference measurements (Tape et al., 2010). Gradients of (ξ) with respect to the solid parameters (ρ_s, C_{IJ}) are obtained by the zero-lag cross-correlations

$$\frac{\partial \xi\,(\mathbf{m})}{\partial \rho_s} = (\bar{\mathbf{u}}, \partial_{tt}\mathbf{u})_{\Omega_s,t}\,; \quad \frac{\partial \xi\,(\mathbf{m})}{\partial C_{IJ}} = \left(\bar{\boldsymbol{\varepsilon}}, \frac{\partial \mathbf{C}}{\partial C_{IJ}}\boldsymbol{\varepsilon}\right)_{\Omega_s,t} \tag{4}$$

where $\bar{\mathbf{u}}$ is the adjoint wavefield vector associated with $\mathbf{u}$, and $\bar{\boldsymbol{\varepsilon}}$ is the adjoint of the strain field $\boldsymbol{\varepsilon}$ for model sets Ω_s.

4.2 Acoustic-Elastic modeling of Scholte-Rayleigh Waves

Since we also invert phase dispersion data for S-wave velocities in the Ligurian-Provence basin, we have to consider the influence of the seafloor topography on the propagation of

surface waves in the 5-20 s period band. Indeed, Scholte waves can be excited as a result of the fluid-solid interaction (e.g., Zheng et al., 2013; J. Zhu et al., 2004). Scholte waves can also be generated from Rayleigh-Scholte mode conversion at the continent-ocean transitions. To further investigate this influence, we account for the effect of the water layer by considering fluid-solid coupling in the 3-D wave equation through the second-order equation system (Cao et al., 2022):

$$\begin{aligned}
&\rho_s \partial_{tt}\mathbf{u} = \nabla\cdot\boldsymbol{\sigma} + \mathbf{f}_s, \quad \boldsymbol{\sigma} = \mathbf{C}\boldsymbol{\varepsilon}, && \text{in } \Omega_s,\\
&\frac{1}{\kappa}\partial_{tt}\varphi - \nabla\cdot\left(\frac{1}{\rho_f}\nabla\varphi\right) = \frac{1}{\kappa}\iint -P_f dt dt, && \text{in } \Omega_f,\\
&\mathbf{u}\cdot\mathbf{n} = \frac{1}{\rho_f}\nabla\varphi\cdot\mathbf{n}, \quad \boldsymbol{\sigma}\cdot\mathbf{n} = \partial_{tt}\varphi\mathbf{n}, && \text{on } \Gamma_{fs}.
\end{aligned} \tag{5}$$

where the first equation describes the elastic wave propagation in the solid domain (Ω_s) in terms of displacement vector $\mathbf{u}$ (same as Eq. 3). The second equation describes the acoustic wave propagation in the fluid domain (Ω_f) in terms of scalar displacement potential φ. P_f is the pressure source associated with a force vector $\mathbf{f}_f$, ρ_s is the fluid density and κ is the bulk modulus of the fluid. The third system gives the boundary conditions along the fluid–solid interface (Γ_{fs}), describing the interaction between the two domains. In our implementation, we consider to discretize the topography of onshore-offshore transition zones through staircase functions to preserve the configuration of structured mesh used in SEM46. We consider a minimum vertical size of 200 m for elements in the water column, ensuring proper sampling of waves in water. Misfit gradients in the solid domain are given by expressions (4). In the fluid domain, gradient building is performed following the hybrid approach proposed by Cao et al. (2022). Gradients of (ξ) with respect to the fluid parameters (ρ_f, κ) are then obtained by the zero-lag cross-correlations:

$$\frac{\partial\xi(\mathbf{m})}{\partial\rho_f} = \left(\nabla\bar{P}, \frac{1}{\rho_f^2}\nabla P\right)_{\Omega_f,t}; \quad \frac{\partial\xi(\mathbf{m})}{\partial\kappa} = \left(\bar{P}, \frac{1}{\kappa^2}\partial_{tt}P\right)_{\Omega_f,t} \tag{6}$$

The gradients on V_p and V_s are estimated using elementary gradients (4) and (6) based on chain rule.

Figure 3 shows snapshots of the simulated vertical displacement recorded at the surface, in the 5-10 s period band for an onshore source station located in southern France. We performed elastic (Figs. 3a1-c1) and acoustic-elastic modeling (Figs. 3a2-c2) in the initial model. Snapshots for the simulation in the 10-20 s period band are shown in the supplementary Fig S1. Figure 4 shows synthetic waveform fits to data at an OBS located in the central Ligurian-Provence basin at a depth of $\sim$ 2700 m (location in Fig. 4a). Fig-

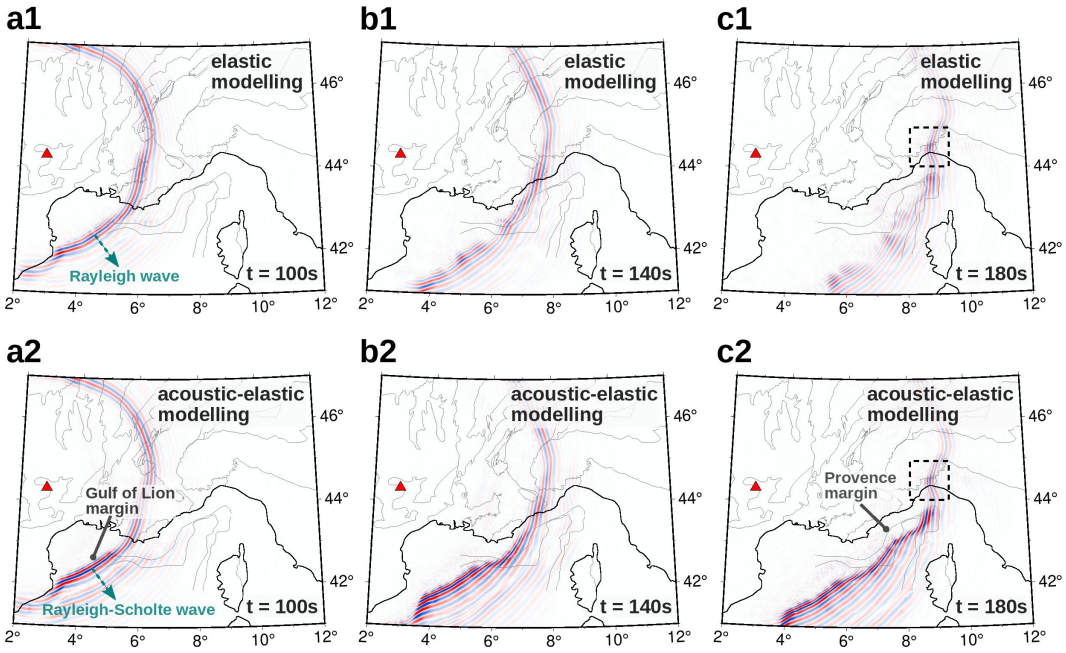

Figure 3. Comparison of snapshots of the vertical displacement wavefield in the 5-10 s period band, simulated using (a1-c1) the elastic wave equation, (a2-c2) the acoustic-elastic coupled wave equation, for the source station indicated by the red triangle. The wave fields are extracted on a 3-D surface corresponding to the topography in the onshore part and to the bathymetry of the seafloor in the marine part. Black dashed frames show scattered Rayleigh-wave packets. The thin black lines are geological and tectonic boundaries from Figure 1.

ures 4b1,b2;c1,c2;d1,d2 show simulations in the initial model and Figs. 4b3,c3,d3 show simulations in the final model. In the elastic modeling case, the source–OBS pair is assumed to be located on the free surface. We therefore observe the propagation of a Rayleigh wave everywhere in the oceanic part (Figs. 3a1-c1). In the acoustic-elastic case, we account for the fluid-solid coupling by considering the presence of the water layer in the Ligurian sea. In this case, we observe a mode conversion from Rayleigh to Rayleigh-Scholte wave at the Gulf of Lion margin (Figs. 3a2-c2). The resulting wave packet is characterized by stronger amplitude and slower propagation velocity and includes strong wavefront distortions. However, we notice in both cases a dissipation within the Ligurian-Provence basin and almost the same wavefield in the continental part, as expected. For instance, both simulations evidence a scattering of the wave packet to the north of the Ligurian sea (dashed black frame in Figs. 2c1,c2). The discrepancies in amplitude and traveltime in the oceanic part are significant. Indeed, the arrival time of the Rayleigh-wave envelope obtained from elastic modeling in the 5-10 s band is $\sim$ 35 s earlier than that of the Rayleigh-Scholte wave obtained from acoustic-elastic modeling (Figs. 4b1-b2). Furthermore, the arrival time of the observed surface wave is much closer to the arrival time of the simulated signal with fluid-solid coupling (Figs. 4b2). This fit is further improved after inversion as shown in Fig. 4b3. Differences between the two modeling results are also visible in the 10-20 s period band with a lower but still significant misfit due to the free-surface boundary condition (Figs. 4c1-c3). As illustrated in Figs. 4d1-d2, the differences between elastic and acoustic-elastic simulations are negligible in the 20-40 s period band, showing that the surface wave in these period ranges becomes insensitive to the coupling effect and presence of water. Furthermore, the waveform computed from elastic modeling in the final model fits very well the observed signal (Fig. 4d3), indicating that the elastic assumption is realistic-enough at long periods.

Figure 5 shows snapshots extracted at the solid surface (topography and seafloor) and at 10 km depth, in the 5-10 s period band for an OBS source located in the northeastern part of the Ligurian-Provence basin. We observe a significant amplitude attenuation at depth of the wave propagating in the Ligurian-Provence and Tyrrhenian basins. This is consistent with the trapping of the Rayleigh-Scholte wave in the vicinity of the elastic-acoustic interface (e.g., Nayfeh, 1995). Hence, we detect the long-period dispersion of the elastic wave at 10 km depth, characterized by less distorted wavefront. Finally, Figure 5 shows that wave packets are dissipated in the oceanic part (Ligurian-Provence and Tyrrhenian basins) or through the sharp Provence margin towards the continental part. This suggests that considering the

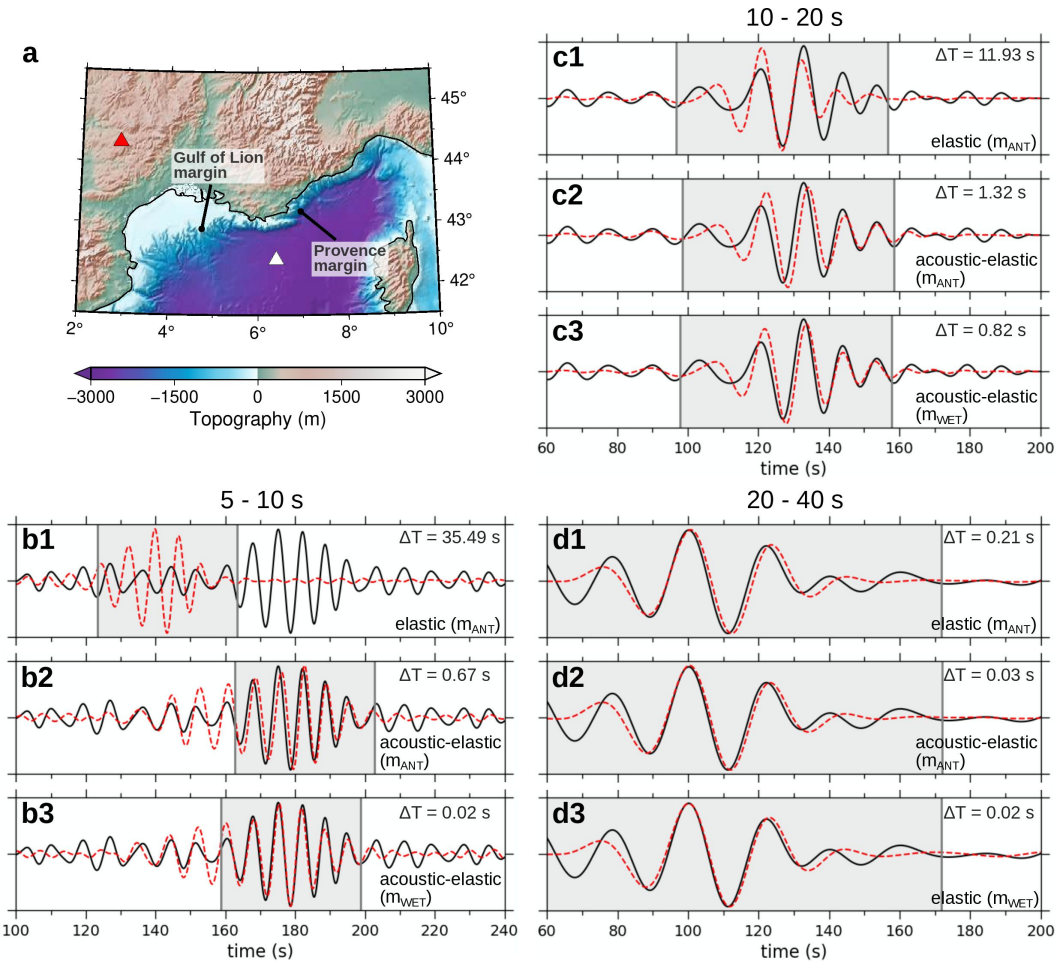

Figure 4. Comparisons between simulated vertical-component seismograms (red) and observed noise correlation waveforms (black), filtered in the 5-10 s, 10-20 s and 20-40 s period bands, for the source-receiver pair in (a) (red: station source, white: receiver). Elastic and acoustic-elastic simulations in the initial model (labeled "m_{ANT}") are shown in b1, c1, d1 and b2, c2, d2 respectively. Seismograms in b3, c3 are computed from acoustic-elastic modeling in the final model (labeled "m_{WET}") while d3 is computed from elastic modeling. The gray areas indicate the surface-wave window and ΔT corresponds to the cross-correlation-based time shift between observed and synthetic windowed waveforms.

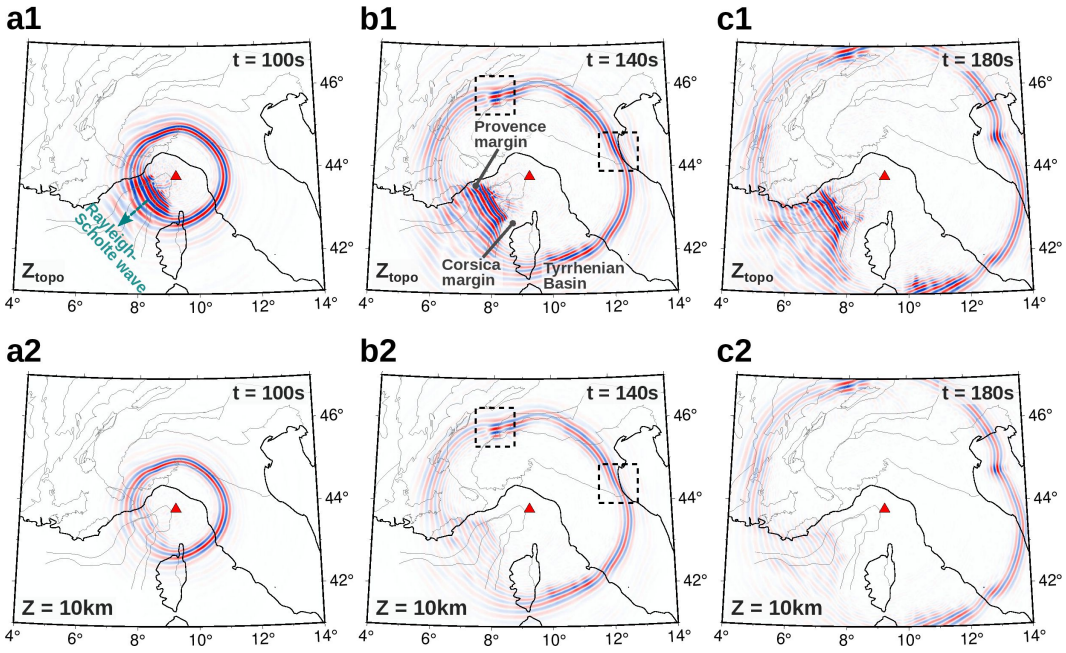

Figure 5. Snapshots of the wavefield computed from the acoustic-elastic coupled wave equation in the 5-10 s period band, showing the depth attenuation of the Rayleigh-Scholte wave generated by an offshore source (red triangle). Wavefields are extracted (a1-c1) at the surface (Z_{topo}, same definition as in Fig. 3) and (a2-c2) at 10 km depth. Black dashed frames show scattered Rayleigh-wave packets.

fluid-solid interaction would help to recover the shallow 3-D velocity structures, as it will be illustrated in the next section.

5 Results and Discussion

As Rayleigh waves from ambient-noise correlations in the period range 5-85 s are mainly sensitive to shear-wave velocities at depth, i.e. the most significant variations from the initial model would occur in V_s, we analyse here depth slices and Moho maps from the obtained 3-D V_s model and discuss their geological implications.

5.1 Depth Slices

Figure 6 shows the depth slices of the initial and final V_s models at 6 km (Figs. 6a1-a2) and 26 km (Figs. 6b1-b2) and corresponding relative variations (Figs. 6a3,b3). We observe a roughly preserved geometry of velocity structures but strong relative variations. At 6 km-

depth, the final model exhibits lower velocities ($\leq$ 2.5 km/s) with strong negative velocity variations (≤ -8 %) in the Ligurian-Provence basin. These low velocities probably reflect the slow propagation of Rayleigh-Scholte waves, induced by the sedimentary cover. Another new pattern appears in Corsica where the western Variscan Corsica (see Fig. 1) exhibits higher velocities ($\geq$ 3.5 km/s) than the northeastern Alpine Corsica. Such variations are probably due to Rayleigh-Scholte mode conversions across the Corsican margin, which are taken into account by the 3-D fluid-solid coupling. On the onshore domain, relative variations roughly coincide with geological structures, with a velocity decrease in the western and eastern parts of the subduction wedge and an increase in the forelands.

The 26-km maps (Figs. 8b1-b3) display two striking features: (1) a velocity decrease (down to -8 %) in the subduction wedge with a northeastward focusing of the low-velocity anomaly (LVZ) beneath the W-Alps, and (2) a velocity increase (up to 8 %) in the crust beneath the Alpine forelands and the Apennines. The transitions between these domains show small variations to the initial model, highlighting the effectiveness of the ANT model in dealing with sharp transitions along the main tectonic boundaries (e.g., the subduction wedge-European foreland boundary, see Fig. 1). We will see in Section 6.1 that such transitions exhibit a low average misfit. Nevertheless, the strong variations in velocity between the ANT and WET models demonstrate the strengths of WET in addressing the high-frequency approximation and 1-D assumption issues associated with the ANT procedure. The comparison with the WET model by Lu et al. (2020) is shown in Supplementary text S1 and Figure S2. The initial and final V_p models remain fairly close due to the limited sensitivity of Rayleigh waves to P-wave velocity (Supplementary Fig. S3).

5.2 Vertical Cross-Sections

We now focus on the western Alpine and Ligurian-Provence regions, and compare the initial and final Vs models along 2-D cross-sections of the crust and uppermost mantle (profiles P1-3 in Fig. 1). These profiles traverse complex geological domains that are well known at the surface and have already been investigated at depth using other techniques with independent data. The underlying three-dimensional structure is therefore particularly interesting for validating the continental and oceanic parts of the model.

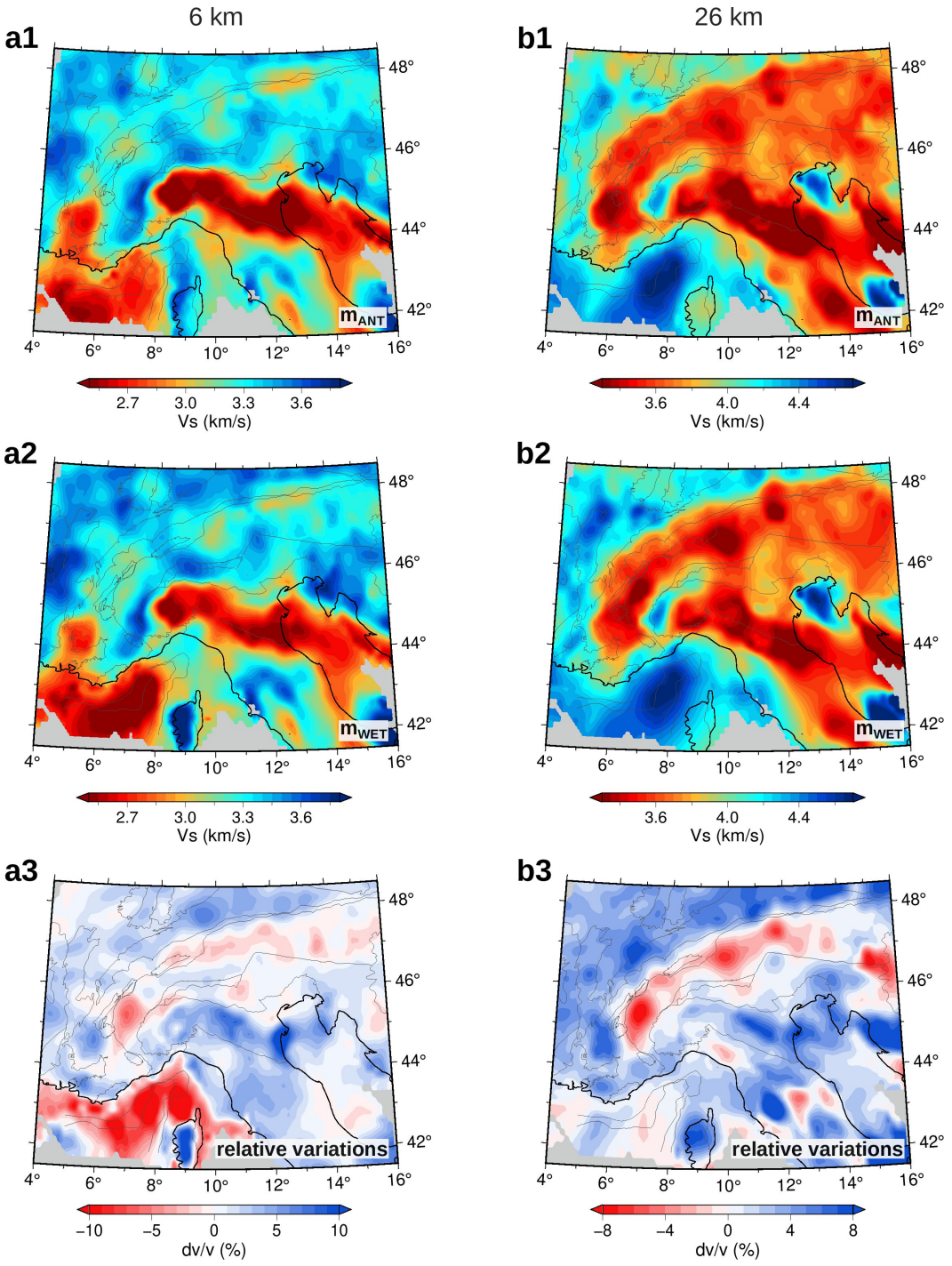

Figure 6. Depth slices in the initial (a1-b1) and final (a2-b2) shear-wave velocity models and the relative variations to the initial model (a3-b3), at 6 km (a1-a3) and 26 km (b1-b3) depths.

5.2.1 Cross-sections in the western Alps

The profile P1 (Fig. 1) coincides with the Cifalps transect, which was extensively investigated in a number of tomographic studies (Malusà et al., 2021, and references herein). The profile P2 is located close to ECORS-CROP wide-angle reflection transect (Nicolas et al., 1990) and Cifalps-2 RFs transect (Paul et al., 2022). The two profiles cross the W-Alps from the European foreland (subducted lower plate) to the Adriatic foreland (upper plate), and the subduction wedge delimited by the Penninic Frontal Thrust (PFT) to the west and the Insubric Fault (IF) to the east (Figs. 7a1-b1).

The cross-sections in initial (ANT) and final (WET) V_s models as well as their relative velocity changes are shown in Figure 7. The final model displays lower velocities in the European mantle and higher velocities in Adria mantle ($\pm$2-3 %). We note a progressive increasing of velocities beneath the subduction wedge, as highlighted by positive-velocity variations from 40 km depth and 180 km offset. Such variations at large depths indicate a significant contribution to the model update from the long-period component of the dispersion data. The European crust (ECC) is marked by an attenuation ($dv/v \geq +5$ % in P1) of the lower crust LVZ (label "1") beneath the foreland, and strengthening ($dv/v \leq -3$-4 %) of the LVZ (label "2") beneath PFT trace. These two velocity changes are already visible in Figure 6, indicating a north-eastwards shift of LVZ1. This shift is likely the result of correcting for a bias from the seismic ray deviation that is not accounted for in the ANT model due to the high-frequency approximation. It also reflects the higher resolution of the final model. The resolution tests in Section 6.4 show that such perturbations are fairly reliable. The final model exhibits smaller changes in Adria crust (ACC), which is less structurally complex than ECC, indicating that it is indeed well constrained at depth by the ANT.

Similarly to RFs Moho (dashed yellow line), the 4.2 km/s contour of the final model dips continuously following the subduction of European lithosphere, reaching a maximum depth of $\sim$ 80 km. In the north (profile P2), the European Moho reaches only 55 km maximum depth, which is consistent with CSS and RFs data along ECORS-CROP and Cifalps-2. We therefore define this contour as proxy for Moho in W-Alps. Below the subduction wedge (profile P1), the Moho geometry is more stable than that of the ANT which extends to depths of more than 90 km (location "3"). Similar changes along P2 underline a decrease in the maximum depth (55 km instead of 70 km). We note strong changes in the V_s gradient at Moho depths, particularly along P2 ($dv/v \geq +5$ %). However, no changes are observed at

the Moho jump in this profile, indicating that this structure is well constrained by the ANT. Finally, the crust-sediment interface, which can be roughly approximated by the 2.8 km/s contour, shows a velocity decrease below the Po plain and below the Rhone valley. Such variations along the main interfaces are likely the result of correcting for a bias from the 1-D assumption in the construction of the ANT model. Moreover, their sharpness undoubtedly demonstrates the resolving capacity of our wave-equation tomography.

5.2.2 Cross-Section in the Ligurian-Provence Basin

We now focus on the offshore part of our study area and discuss the P3 profile along the axis of the Ligurian-Provence basin (location in Fig. 1). This transect crosses the three main domains involved in the genesis of oceanic crust. The oceanic southwestern part of the transect coincides with the seismic refraction and wide-angle reflection line by Dannowski et al. (2020), while the northeastern part coincides with the marine part of the wide-angle reflection line by Makris et al. (1999).

Figure 8 shows that the final model displays major velocity changes with respect to the ANT model: (i) strong decrease in sediments and crust of the oceanic domain ($dv/v \geq -8$ %); (ii) strong increase in sediments and decrease in crust of the transitional domain; (iii) decrease in sediments and crust of the southwestern margin domain, and an increase to the north-est. Such changes at shallow depths are likely related to the consideration of 3-D fluid-solid coupling. Conversely, the uppermost mantle displays lower velocity changes with an overall decrease in the oceanic domain and an increase in the transitional and continental domains. Similarly to Nouibat et al. (2022b), we define the Moho proxy as the 4.1 km/s contour which is the more consistent with the V_p Moho proxy defined as the 7.3 km/s V_p contour by Dannowski et al. (2020) (dashed yellow line). Depth and geometry of the Moho proxy are almost unchanged in the oceanic part. However, we observe a significant increase in velocity reflecting a stronger gradient at this interface, similar to Moho in W-Alps. Finally, we observe a shallower Moho in the final model at the transition to the margin.

5.3 New large-scale map of Moho depth

In a tectonically complex setting as in the Alps and Northwestern Mediterranean, a precise definition of the three-dimensional Moho structure is fundamental to understand the link between mantle dynamics and the geological setting.

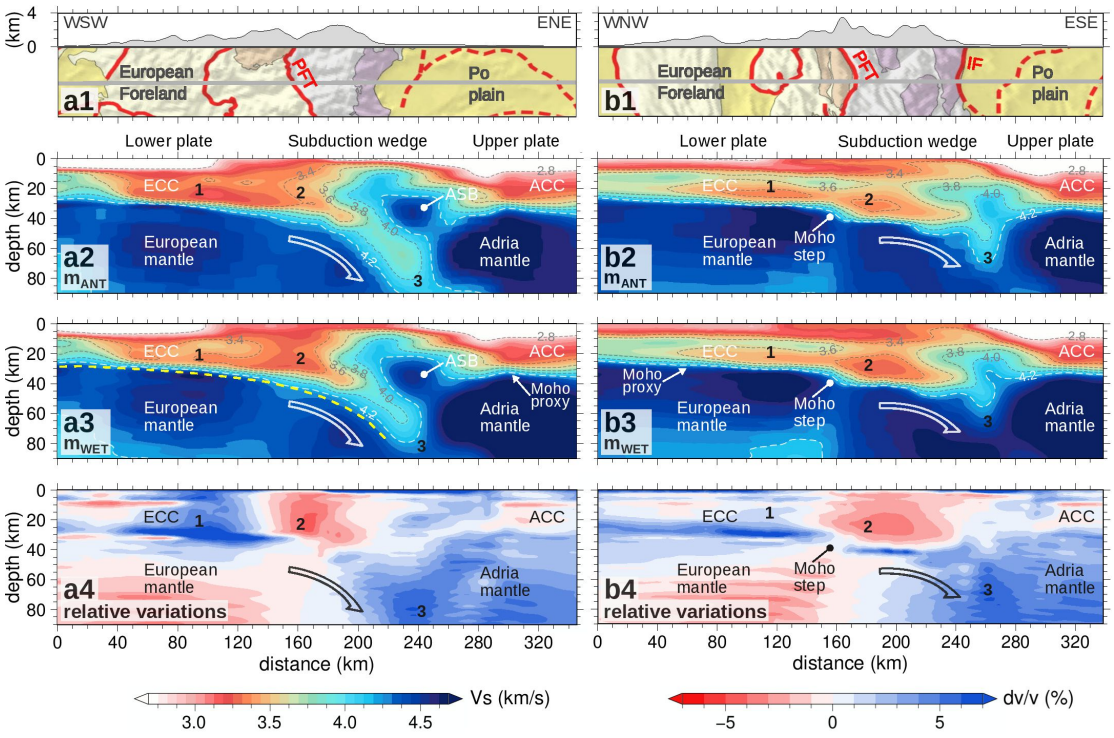

Figure 7. Comparison of depth sections for the initial and final models along the WSW-ENE transect P1 (left-hand side) and the WNW-ESE transect P2 (right-hand side). Locations of P1 and P2 are indicated in Figure 1. (a1-b1) Topographic profiles and geological maps (extracted from Fig. 1). (a2-b2) Shear-wave velocities from the ANT initial model ("m_{ANT}"). (a3-b3) Shear-wave velocities from the WET final model ("m_{WET}"). (a4-b4) Relative variations to the initial model. The white and black curved arrows highlight the subduction of the European lithosphere beneath Adria. The dashed yellow line in (a3) show the European Moho picked from a receiver functions section (Zhao et al., 2015). Note the remarkable agreement with the V_s Moho proxy in (a3). Acronyms: ECC, European continental crust; ACC, Adria continental crust; ASB, Adria seismic body (Nouibat et al., 2022a). Labels 1, 2 and 3 indicate velocity structures discussed in the text.

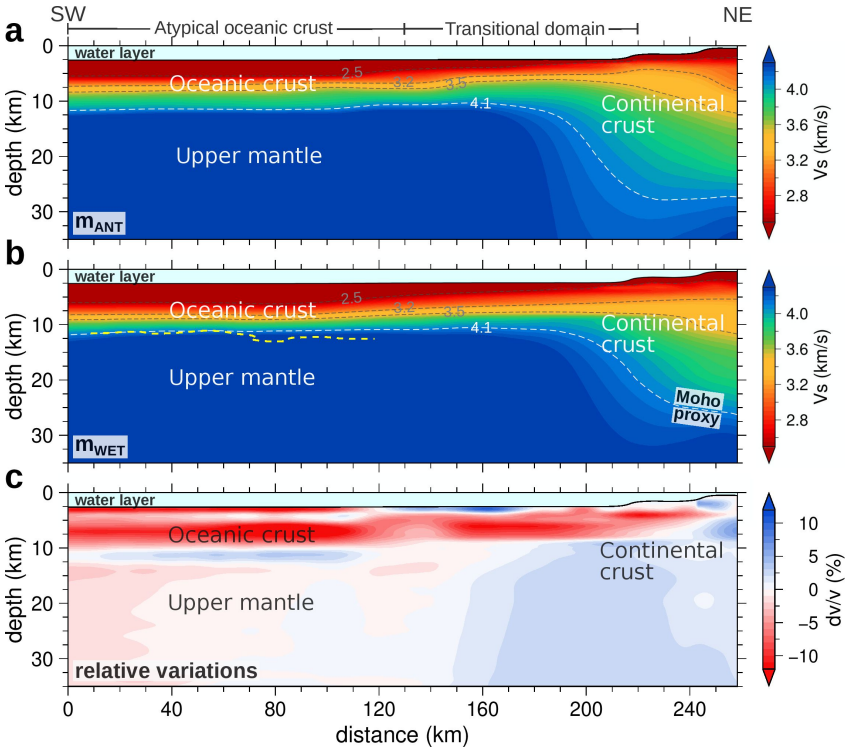

Figure 8. Comparison of depth sections for the initial and final models along the SW-NE offshore transect P3 (see location in Fig. 1). (a) Shear-wave velocities from the ANT initial model. (b) Shear-wave velocities from the WET final model. The yellow dashed line represents the Moho proxy from the active seismic P-wave velocity section of (Dannowski et al., 2020). (c) Relative variations to the initial model.

The Moho depth cartography in the Alpine region has been the target of a variety of seismological methods, such as interpolating data from CSS, RFs and LET (Fig. 9a; Waldhauser et al., 1998; Lombardi et al., 2008; Piana Agostinetti & Amato, 2009; Diehl et al., 2009; Di Stefano et al., 2009; Spada et al., 2013), conventional ANT (e.g., Molinari & Morelli, 2011; Kästle et al., 2018; Lu et al., 2018) and more recently from WET (Fig. 9b; Lu et al., 2020). Zhao et al. (2015) showed the first evidence of continental subduction beneath the western Alps obtained by analyzing receiver functions along the Cifalps-1 seismic profile. By using simultaneously observations from receiver functions across the Cifalps-1 and Cifalps-2 profiles and the V_s model by Nouibat et al. (2022a), Paul et al. (2022) documented a marked change in the depth of the European Moho from north to south of the western Alps, which occurs over a distance of a few tens of kilometers only.

In this section, we present a new 3-D Moho map at the scale of the Alps and Northwestern Mediterranean (Fig. 9c). The Moho depth is estimated from the depth of the iso-velocity surface $V_s = 4.2$ km/s. In the western Alps, our 3-D map of the Moho is overall similar to the one obtained by Lu et al. (2020), with some important discrepancies (Figs. 9b-c). In the southwestern Alps, while Lu et al. (2020)'s model exhibits $\sim$ 40-45 km depths, the European Moho in our model deepens to depth greater than 60 km (see Fig. 7), which is more consistent with the continental subduction from RF observations (Zhao et al., 2015). Using the iso-velocity 4.2 km/s as a proxy, we obtain a shallower Moho (20-25 km) associated with the Ivrea Body (white dashed line on Fig. 9c). The strong along-strike variations in our Moho depth from north to south are in line wih RF observations between the northwestern and southern Alps (Paul et al., 2022), indicating a non-cylindricity of the deep structure of the western Alps. Besides these differences, we observe a similar Moho topography than Lu et al. (2020). In particular, we observe a Moho jump below the external crystalline massifs that in our model appear to be linear and aligned with the Variscan Accident (arrows on Fig. 9b-c).

5.4 Moho topography beneath the Ligurian sea

3-D crustal imaging of oceanic domains based on ambient-noise surface waves is a challenging topic due to the difficulty of accounting for effects of the water layer and complex seabed relief in a hybrid medium, as illustrated in this study. One of the main objectives of this study is to produce an homogeneous 3-D map of the Ligurian Moho in line with the physics of surface-wave propagation.

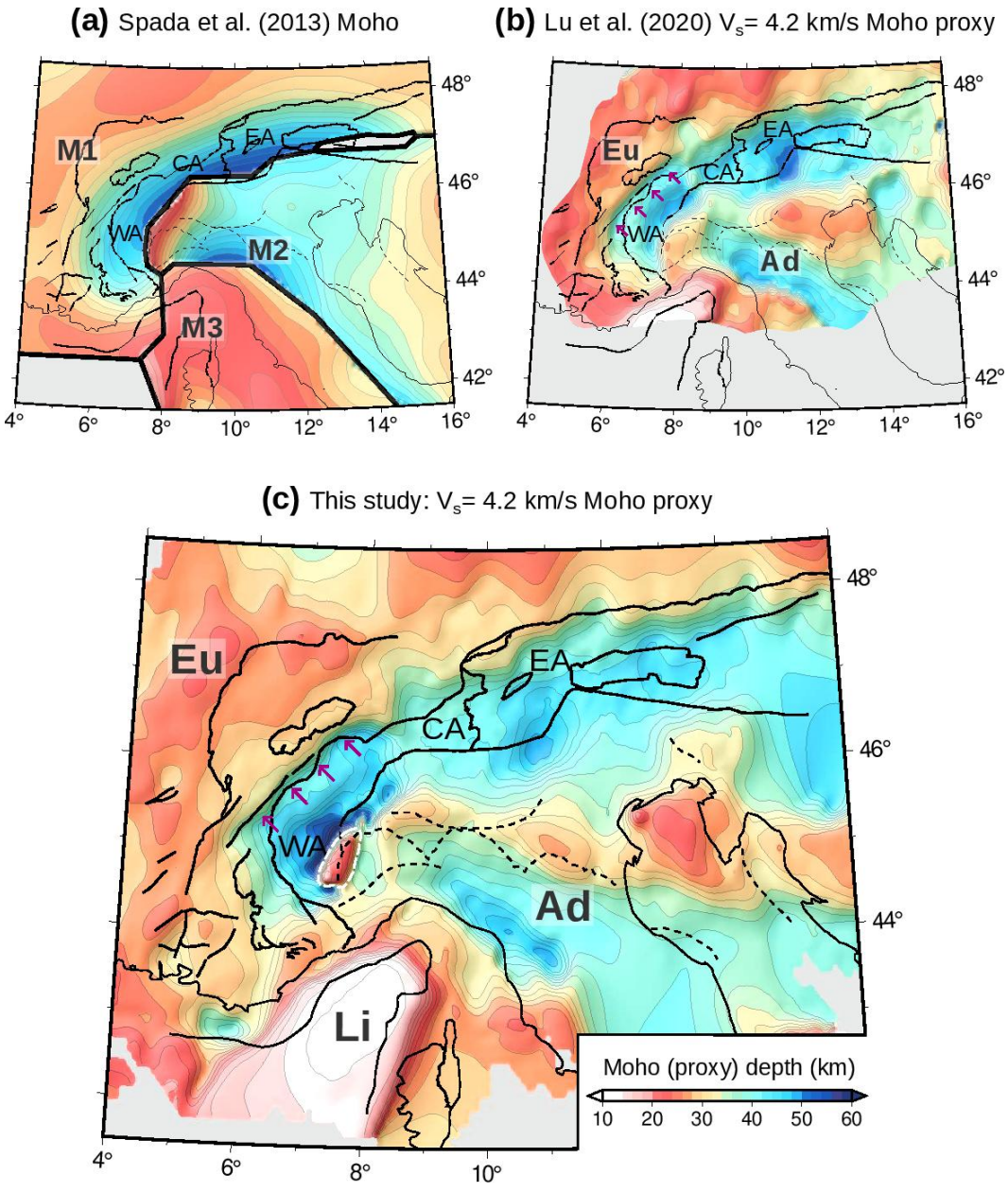

Figure 9. Depth maps of Moho and Moho proxy in the Alps and Northwestern Mediterranean. (a) Spada et al. (2013)'s map composed of three blocks: European Moho (M1), Adriatic Moho (M2) and Ligurian–Sardinia–Corsica–Tyrrhenian Moho (M3). (b) Lu et al. (2020)'s depth map of the $V_s = 4.2$ km/s iso-velocity surface from their WET model. (c) Depth map of the $V_s = 4.2$ km/s iso-velocity surface from our WET model. For a better illustration, the color scale is saturated at 60 km depth; Our model shows 70-75 km depths in the southwestern Alps (continental subduction; see Fig. 7). Acronyms: Eu, European Moho; Ad, Adriatic Moho; Li, Ligurian Moho; WA, Western Alps; CA, Central Alps; EA, Eastern Alps. Arrows in purple: Moho step beneath the external crystalline massifs (Lu et al., 2018). Dashed white line: shallow Moho associated with the Ivrea Body. The gray areas hide regions where Moho maps are unconstrained.

Unlike the Alpine region, the 3-D structure of Moho in the Ligurian sea is poorly constrained by 3-D velocity models. In this region, the few constraints on the Moho depth are mainly provided by CSS data (e.g., Makris et al., 1999; Rollet et al., 2002; Contrucci et al., 2001; Dannowski et al., 2020). This gap is partly due to the poor coverage of seismological stations in this area before the deployment of AlpArray OBSs, making it difficult to achieve 3-D high-resolution imaging with tomography methods such as ANT or LET.

Figure 10 shows the Moho depth map in the Ligurian-Provence basin estimated from the iso-velocity surface V_s=4.1 km/s. The Moho map shows strong lateral variations with depths, ranging from 12 km in the axis of the basin to $\sim$ 20-25 km in the conjugate margins of Provence and Corsica. The transition to the Ligurian-Provence and Corsica margins is characterised by a strong gradient in Moho depth while the transition to the Ligurian margin is smoother. In the oceanic domain, the Moho gradually deepens along the axis of the basin, from 12 km in the northern and central parts to $\sim$ 14-18 km in the southern part. Red dashed show depth contours of a recently published Moho surface from conventional ANT (Magrini et al., 2022). This map shows smoother depth variations than ours within the basin and at transitions to the conjugate margins. Along the basin axis, it shows depths increase from the southern part (15 km) to the northern part (18 km) of the basin. While our Moho has a depth of about 12 km in the oceanic domain traversed by the active seismic profile of Dannowski et al. (2020), the Magrini et al. (2022)'s Moho is 15-18 km deep in the northern portion of the profile and more than 18 km deep in the southern portion. However, Dannowski et al. (2020) detected a Moho of $\sim$ 12 km depth, which is more consistent with the depths displayed by our model (see Fig. 8). These comparisons demonstrate that our Moho model provides a better resolution of the crustal thinning beneath the Ligurian-Provence basin.

6 Model robustness

In this section, we will document the robustness of our resulting velocity model. First, we analyse the distribution of phase traveltime misfits of surface waves from the ambient-noise database used in this study. Then, we validate our model with earthquake seismic waves in the western Alps, (1) by comparing P-, Rayleigh-wave observed waveforms with synthetic waveforms computed in our model, and (2) by analysing the distribution of first-

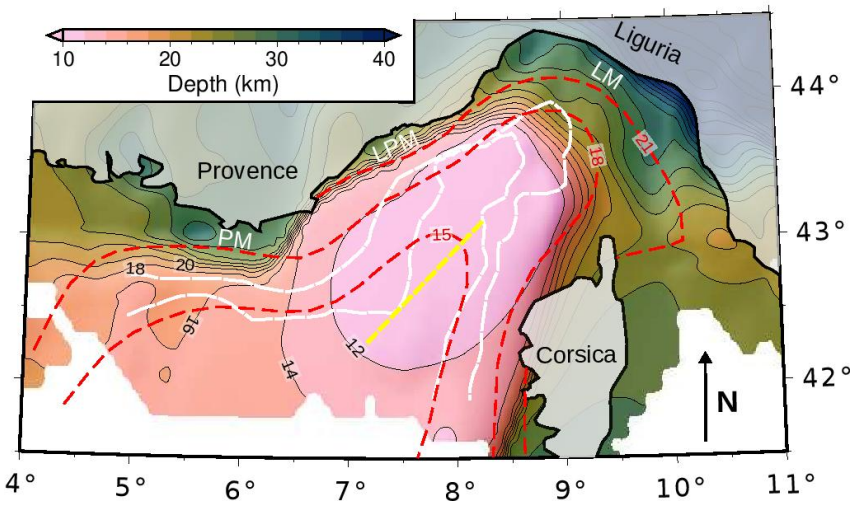

Figure 10. Depth map of the $V_s = 4.1$ km/s iso-velocity surface from our WET model as a proxy of Moho in Northwestern Mediterranean. Black lines are iso-depth contours from our Moho proxy. Red lines: iso-depth contours from Magrini et al. (2022). Dashed yellow line shows the trace of Dannowski et al. (2020)'s CSS profile. Dashed white lines are limits of the main geological domains in the Ligurian-Provence basin from Rollet et al. (2002). Acronyms: PM, Provence margin; LPM, Ligurian-Provence margin; LM, Ligurian margin.

arrival traveltime residuals between picked P, S arrivals and synthetic arrivals predicted in our model.

6.1 Misfit Analysis

We first document the model robustness by analyzing histograms of misfit for the initial and final model and their spatial and azimuthal distributions. The misfit is expressed as traveltime delay for waves propagating on 100-km distance (s/100km) in order to avoid biases related to long inter-station distances. Figure 11 shows histograms of traveltime misfits for the initial (in red) and final (in blue) models at 8, 20, 35 and 35 s period. The mean and standard deviation of the misfit distribution allow a quantitative comparison. The initial histograms are rather narrow and globally centred around zero misfit value (absolute misfit ≤ 0.1 s/100km). The initial standard deviation increases with period (0.3 s/100km at 8 s to 0.73 s/100km at 55 s). We do not observe a significant shift of the mean value, which illustrates the consistency of our ANT model. Since our initial model does not suffer from biases towards wrong mean-value velocities, our inversion further contributes in refining the

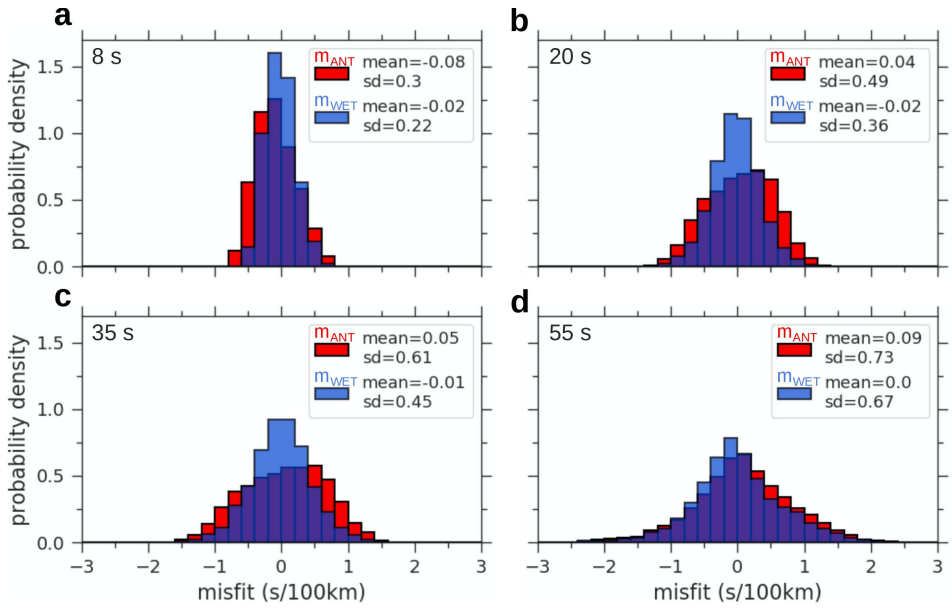

Figure 11. Comparison of histograms of misfit (in s/100km inter-station distance) for the initial (m_{ANT}, red) and final (m_{WET}, blue) velocity models at 8, 20, 35 and 55 s periods. Labels "mean" and "sd" refer respectively to the mean value and standard deviation of the misfit distribution.

intrinsic shape and magnitude of velocity structures rather than the overall mean velocity at depth. The final model fits the data significantly better than the initial model, with overall smaller average misfits and standard deviations. Histograms of cross-correlation type traveltime differences are shown in supplementary Figure S4.

Figure 12 shows misfit maps at 8, 20, 35 and 55 s periods, obtained by averaging misfit values for the initial and final models over $0.2° \times 0.2°$ cells assuming great-circle ray paths. The spatial distribution of the misfit allows to see whether some part of the model are better constrained than others. Positive misfit values mean that the velocity is underestimated, while negative values mean that the velocity is overestimated. In the initial model (Figs. 12a1-d1), the misfit patterns tend to coincide with geological structures due to imperfections in the isotropic initial velocity model. The 8-s map (Fig. 12a1) exhibits rather small misfit values along the central and eastern Alps, west Po basin, southeastern French foreland and the central Ligurian-Provence basin. Stronger negative values are observed in the northeast French foreland, north and south Apennines, and in the northern and western parts of the Ligurian-Provence basin. Besides this, we observe a strong positive anomaly in the Adriatic sea. The 20-s and 35-s misfit maps (Figs. 12b1-c1) evidence positive

misfits all around the Alpine belt, while negative misfits are observed in the Alpine arc and west Po basin. Note that the western boundary of the Alps has rather low misfit values (absolute misfit < 0.4 s/100km) which indicates that the 1-D inversion in the ANT model is sufficiently robust to recover such structural changes at depth. The transition to 55 s is marked by an inversion of polarity: the European foreland and central-western Ligurian-Provence basin evidence negative anomalies, while the central and eastern Alps and Apennines display positive anomalies. Strong negative anomalies are observed in the western Ligurian-Provence basin and central Adriatic sea. Most of these regionally organized misfit patterns are corrected after WET inversion (Figs. 12a2-d2). Although the strong misfits in the south of the study region are significantly smaller, some residuals remain, in particular along boundaries of the study region where path coverage is poorer (e.g., southern Corsica, in the 20-s and 35-s maps, or in the western Ligurian-Provence basin at 55 s). The azimuthal distribution of misfit for the initial and final models is shown in supplementary text S2 and Figure S5.

6.2 Validation with earthquake waveform modeling

We validate our final (V_p, V_s) model by performing 3-D wave propagation simulations of earthquakes in Western Alps. The synthetic waveforms are simulated up to 1 Hz using the same spectral-element-based solver described in section 4. Since the absolute waveform amplitude can be affected by the attenuation quality factors (Q_p, Q_s) at such high frequencies, and we are interested in comparing both amplitudes and phases between observed and simulated waveforms, we consider here a visco-elastic wave propagation. The model is discretized with an adaptive mesh built in the Cartesian system. We parametrize the GLL points with isotropic V_p, V_s from our model, and isotropic ρ, Q_p, Q_s computed from these velocities by empirical formulas (Brocher, 2005). We represent the earthquakes as a moment source, using moment tensor solutions obtained by Petersen et al. (2021) from centroid moment tensor (CMT) inversion using the AlpArray network. We perform simulations using a Gaussian source-time function with half duration determined by the seismic moment (Komatitsch & Tromp, 2002). The seismograms are filtered in three narrow period bands (2-5 s, 3-7 s and 5-10 s) and the time windows are defined as $[t_{max} - T, t_{max} + T]$ for the P wave-packet and $[t_{max} - 1.5T, t_{max} + 1.5T]$ for the Rayleigh wave-packet, where T is the maximum period of measurement and t_{max} is the maximum envelope arrival time. t_{max} is detected in velocity range for P waves (5.0-8.0 km/s) and for Rayleigh waves (1.5-3.5 km/s). Finally, we mea-

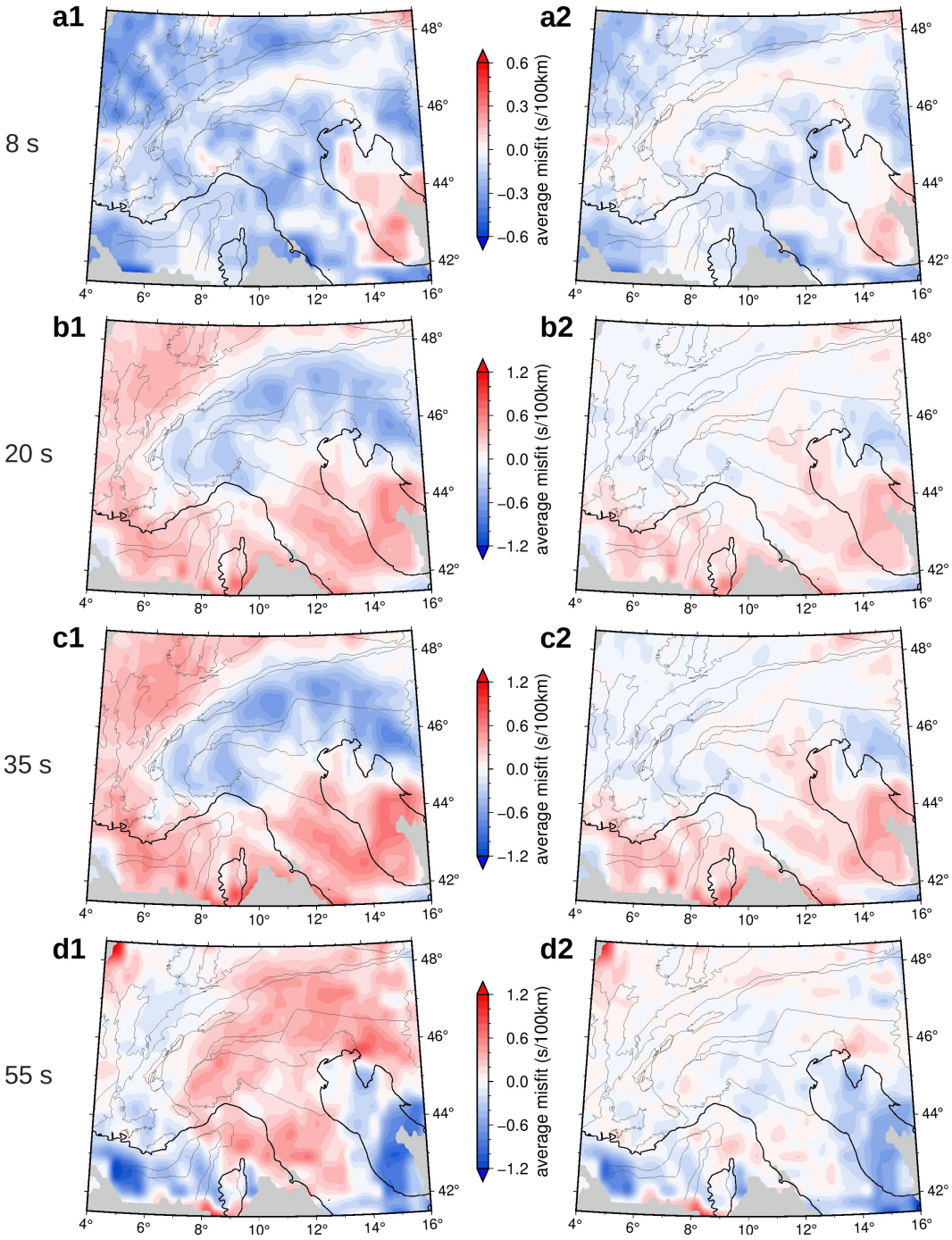

Figure 12. Comparison of the spatial distributions of misfit for the initial (left-hand side: a1-d1) and final (right-hand side: a2-d2) velocity models at 8, 20, 35 and 55 s periods. Misfits are averaged over cells of 0.2° × 0.2° assuming great circle ray paths. The gray area hides regions where the initial model is unconstrained.

sure the cross-correlation-based time shifts to quantify the mismatch between the synthetic waveforms and observations.

Figure 13 shows an example of a comparison between synthetic and observed waveforms for an earthquake of magnitude $M_w = 4$ and 5-km depth that occurred in North Western Alps in 2017 (Fig. 13a for location). The seismograms are recorded by 6 stations from permanent networks (FR, France; CH, Switzerland; GU, Italy) and the temporary AlpArray network (Z3). We observe a striking fit between synthetic and observed waveforms for both P and Rayleigh waves, as supported by an overall time delay lower than 0.65 s (Fig. 13b-c-d). As we expect, the Rayleigh waves are quite well fitted in the 5-10 s period band (Fig. 13d), which is the shorter period band used in our inversion. Besides that, the striking fit in the 3-7 s period (Fig. 13c) highlights the potential of our model to recover the shallower and lateral small-scale structures. The good coherency in phase and amplitude for the P waves in the 2-5 s and 3-7 s period bands (Fig. 13b-c) highlights the potential of our model to recover the small-scale intra-crustal structures. This example illustrates that our WET model could be a relevant starting model for wave-equation tomography of regional earthquake body and surface waves – a natural extension of the wave-equation tomography of ambient noise correlations. A more comprehensive validation of this model will be the subject of a future publication.

6.3 Validation with first-arrival traveltimes of local earthquakes

We further document the robustness of our final velocity model by comparing observed and synthetic body-wave traveltimes associated with more than 75×10^3 earthquakes in the region of Western Alps, over a period of more than 30 years (Fig. 12a). We use $\sim 1.6 \times 10^6$ picked times (93×10^4 P-wave picks and 66×10^4 S-wave picks) coming from the dataset of Potin (2016) for the period between 1989 and 2014, complemented by picked times available from the European plate observing system (EPOS) for the period 2015-2021.

The velocity models are discretized according to a regular Cartesian grid of 5 km cell size in horizontal directions and 2 km in the vertical direction. Hypocenters are relocated in our velocity models using the NLLOC software (Lomax et al., 2000). Initial first-arrival traveltimes are predicted in our 3-D V_s and V_p final models through an efficient eikonal solver (Podvin & Lecomte, 1991) on a finer interpolated square grid of 2 km. Using receivers as eikonal sources saves computer resources, and, therefore, back-tracing rays between each

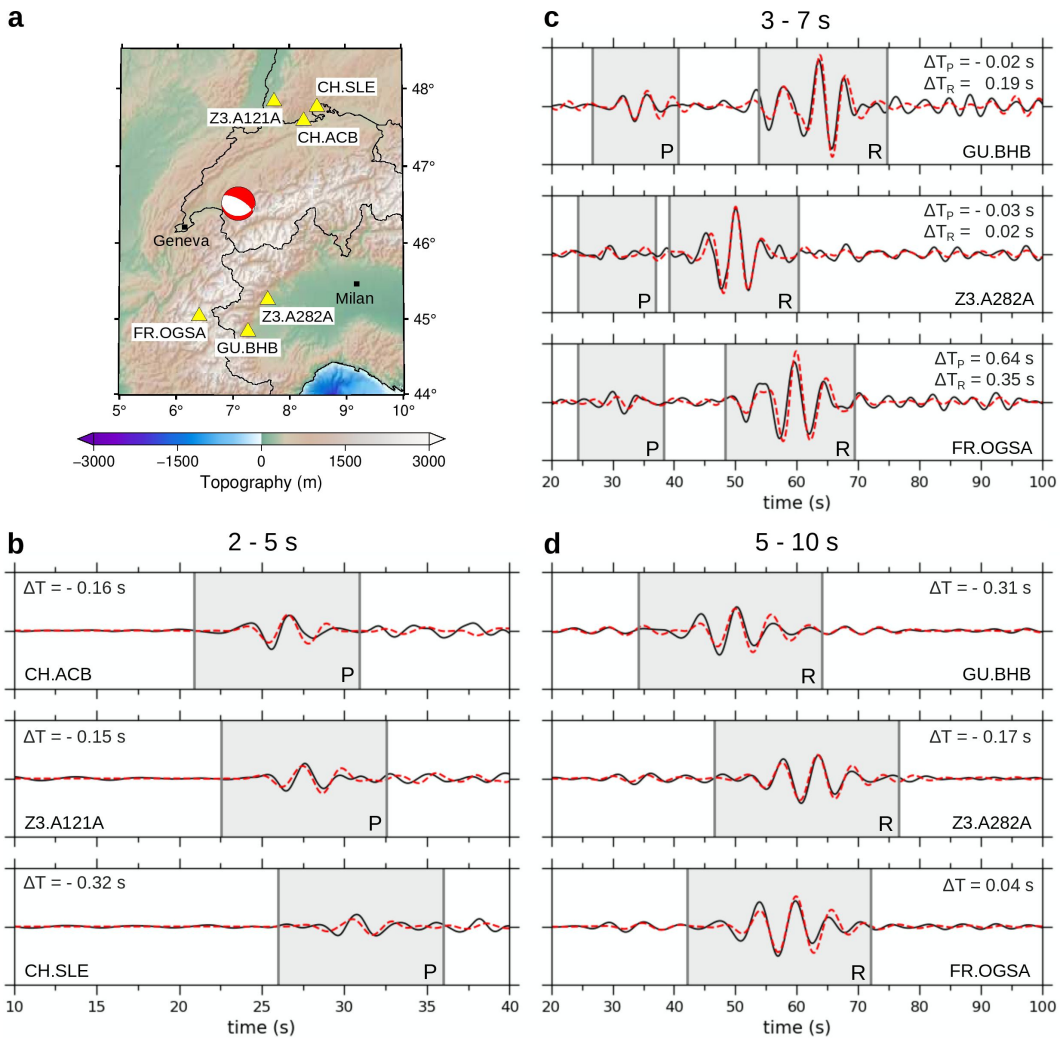

Figure 13. Comparisons between simulated vertical-component seismograms (red) in the WET model and observed waveforms (black), filtered in the 2-5 s, 3-7 s and 5-10 s period bands for the earthquake and receivers in (a) (red: earthquake, yellow: receiver). The gray areas indicate the P-wave (P) and Rayleigh-wave (R) windows and ΔT corresponds to the cross-correlation-based time shift between observed and synthetic windowed waveforms (ΔT_P and ΔT_R respectively for P-, Rayleigh -wave time shifts).

couple (source, receiver) are obtained. Finally, traveltimes are estimated along these rays with a ray sampling of 0.5 km in order to achieve higher-computational accuracy. Using the same procedure, we calculate traveltimes in a 3-D model obtained from a local earthquake tomography using the same dataset (Virieux et al., 2023).

The P and S residuals from our model (blue histograms in Fig. 14b-c) show normal distribution shapes that are rather narrow (standard deviation < 1 s/100km) and remarkably well centred around zero misfit (mean < 0.15 s/100km). The standard deviation of the S residuals is slightly larger, but it should be noted that the total number of P picks is almost 1.4 times larger. However, the mean value of the S distribution is smaller. Such small mean values indicate that our model does not suffer from biases towards wrong mean-value velocities. These histograms obtained from a completely independent dataset are comparable to those in Figure 11 based on surface waves from ambient noise. To further assess the relevance of our model, we compare with residuals from the LET model (red histograms in Fig. 14b-c). The distribution of residuals from our model is notably narrower than that of the LET model. The overall good agreement between observed first-arrival traveltimes and those predicted in our model indicates that it is an accurate enough initial model for 3-D local earthquake tomography. Since it has been obtained using ambient-noise surface waves, this model has the advantage to constrain the lower crust that is often poorly sampled by earthquakes.

6.4 Resolution tests

We perform 3-D spike tests to evaluate the resolution of the final V_s model. Three spikes of ~ 25 km radius and ~ 20 km thickness are located in the crust, beneath Western Alps, Central Alps and northern Ligurian-Provence basin (Fig. 15a1). A spike of ~ 50 km radius and ~ 40 km thickness is located in the uppermost mantle beneath the northwestern Po basin (Fig. 15a2). Theses patterns correspond to velocity perturbations of up to ~ 8 % in the crust and ~ 5 % in the uppermost mantle, with respect to the initial model. Using the same station-pair coverage as our observations, we apply the methodology described in Section 3. Inversion results are shown in the right-hand panel of Figure 15.

At 20 km depth, the crustal anomalies are well recovered. Overall, the shape of the anomalies appears to be slightly stretched. At 50 km depth, the perturbation is recovered but its shape is affected by a strong eastward horizontal smearing. The peak amplitude is

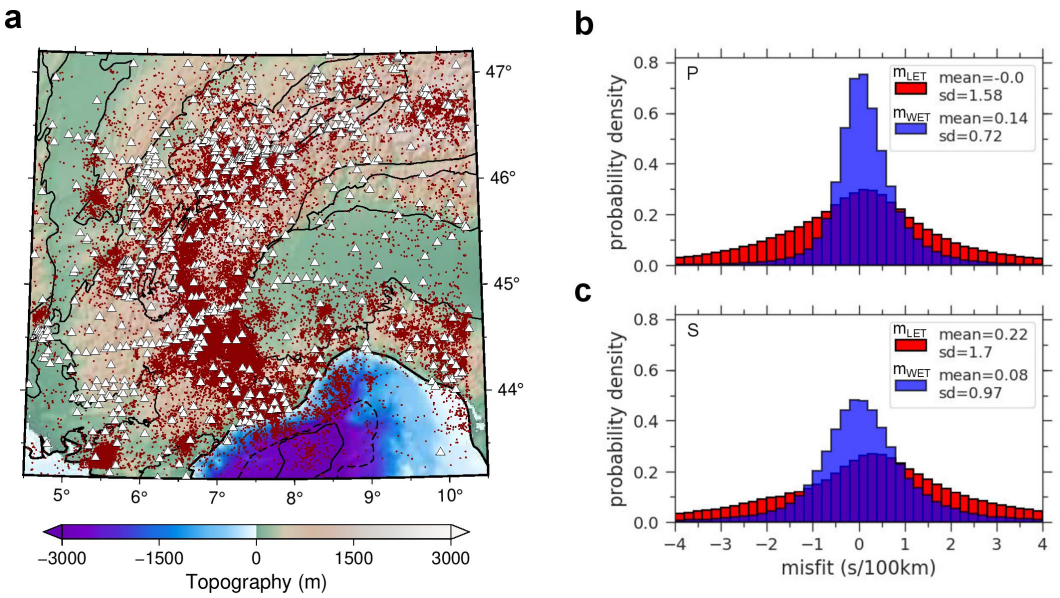

Figure 14. (a) Location map of the seismic events (red dots) and stations (white triangles) constituting the database of first-arrival traveltimes described in section 6.3. (b,c) Histograms of the traveltime residuals for the P waves (b) and the S waves (c) between observations and predicted synthetic arrivals from our velocity model (m_{WET}, blue) and from the LET model (m_{LET}, red). Labels "mean" and "sd" refer respectively to the mean value and standard deviation of the misfit distribution.

weaker as for the crustal anomalies. In both cases, the recovered peak is approximately in the right position. The cross-sections (Figs. 15a3-b3) show that most of the smearing occurs in the horizontal direction. The discrepancies between input and recovered patterns are mainly due to path coverage, to the propagation of Rayleigh wave which induces lateral smoothing of heterogeneities in the crust and upper mantle, and to its sensitivity to the medium which decreases with depth. Nevertheless, part of these discrepancies is also attributable to the tomographic method itself and the convergence rate.

Though these spike tests do not stand for the entire study area, they indicate that our model is fairly resolved in the crust and can be used for the geological interpretation of the three-dimensional geometry of crustal structures and for their petrophysical characterization. While the resolution in upper mantle remains tolerable for a first-order geological interpretation, it is obviously not sufficient for precise petrophysical characterization.

7 Conclusion

Using ambient noise data from exhaustive coverage of permanent and temporary arrays in the western European region, we derive a 3-D onshore-offshore velocity model covering the Alps and Ligurian-Provence basin, using wave-equation tomography (WET). We iteratively refine the recent ANT model of Nouibat et al. (2022a) by minimizing the phase traveltime differences between observed and simulated Rayleigh-wave waveforms in the 5-85 s period band. Observed signals are obtained from ambient noise cross-correlations and synthetics are computed from SEM-based 3-D elastic and acoustic-elastic modeling of surface waves. The specificity of this study is to highlight the effect of the water layer on the 3-D propagation of Rayleigh waves by applying a fluid-solid coupling for 3-D acoustic-elastic simulations, taking the Ligurian sea domain as an illustration. We demonstrate that the elastic propagation assumption is no longer valid at short periods (5-20 s), since the surface-wave packet is dominated by a composite Rayleigh-Scholte mode propagating with lower velocities. Finally, we incorporate the fluid-solid coupling in the inversion framework of the WET.

In line with the true physics of surface-wave propagation, the WET corrects for the biases in the ANT model related to the high-frequency assumption and the 1-D inversion. The resulting model has a better resolution, with significant intra-crustal changes. In the superficial part, the WET better emphasizes the sediments of the Ligurian-Provence domain and a high-velocity anomaly beneath the Variscan part of Corsica. This improvement is

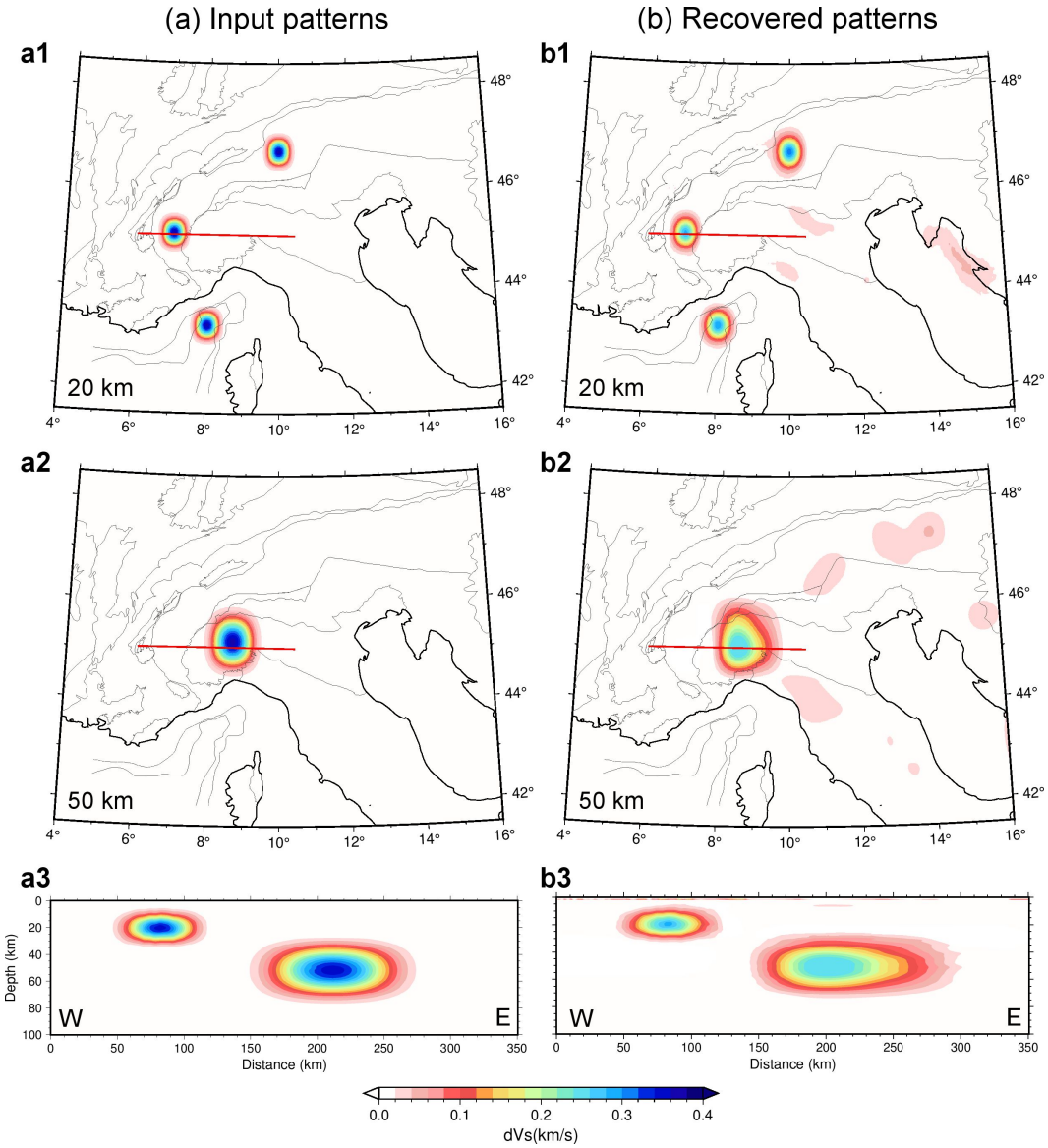

Figure 15. Resolution assessment of the WET V_s model using 3-D spike tests. Left: input perturbations with respect to the initial model (m_{ANT}), right: recovered perturbations. (a1-b1) 20 km depth slices. (a2-b2) 50 km depth slices. (a3-b3) E-W cross-section (red profile in the depth slices).

partly due to accounting for Rayleigh-Scholte wave 3-D sensitivity kernels at short periods. In the crust, the WET mainly change the velocity contrast with an overall velocity decrease in the subduction wedge, focusing the LVZ in the W-Alps to the northeast, and an overall increase in the two forelands. In addition, the WET validates major structures already present in the initial model, such as the subduction of the European crust beneath Adria in the southwestern Alps, and the slow anomalies at the base of the crust in the northwestern Alps, thus validating recent first-order interpretations on the deep structure in this area (e.g., Nouibat et al., 2022a; Paul et al., 2022). Significant changes are observed in the oceanic crust of the Ligurian-Provence domain, where intra-crustal velocities decrease significantly along the axis of the basin.

We present a new depth map of the Moho proxy of Western Europe. In the western Alps, this model shows the deepening of the European crust and confirms the Moho jump under the outer crystalline massifs (Lu et al., 2020) and the high-velocity anomalies associated with the Ivrea Body (Nouibat et al., 2022a). This proxy is the first truly 3-D representation of the land-sea Moho in the Alps and Northwestern Mediterranean. We show a strong deepening of the Moho towards the Ligurian-Provence and Corsica conjugate margins (from 12 to 20-25 km), and a smoother deepening towards the Ligurian margin and the southern part of the basin (from 12 to 14-18 km).

We validated our tomographic model with independent data, through 3-D waveform modeling and first-arrival traveltimes of seismic waves from earthquakes in the region of Western Alps. In a future perspective, this model can be used as a starting model for 3-D imaging based on earthquake data (local earthquake tomography, wave-equation tomography or full waveform inversion) to derive a higher resolution V_p and V_s models of Western Alps and Ligurian sea.

Open Research

Waveform data used in this paper are available through the EIDA (European Integrated Data Archive) service of ORFEUS (http://www.orfeus-eu.org/eida/) and belong to the permanent networks with codes AC, BE (Royal Observatory Of Belgium, 1985), CA (Institut Cartogràfic I Geològic De Catalunya - Institut D'Estudis Catalans, 1984), CH (Swiss Seismological Service (SED) At ETH Zurich, 1983), CR (University Of Zagreb, 2001), CZ (Institute Of Geophysics Of The Academy Of Sciences Of The Czech Republic, 1973), ES

(Instituto Geografico Nacional, Spain, 1999), FR (RESIF, 1995), G (Institut de Physique du Globe de Paris (IPGP) & Ecole et Observatoire des Sciences de la Terre de Strasbourg (EOST), 1982), GB (GEOFON Data Centre, 1993), GR (Federal Institute for Geosciences & Natural Resources (BGR), 1976), IV (INGV Seismological Data Centre, 2006), NL (KNMI, 1993), OE (ZAMG-Zentralanstalt Für Meterologie Und Geodynamik, 1987), SL (Slovenian Environment Agency, 2001), and UP (SNSN, 1904). We also used data of the temporary AlpArray network (network code Z3, AlpArray Seismic Network, 2015), Cifalps-2 experiments (network code XT, Zhao et al., 2018) and EASI experiments (network code XT, AlpArray Seismic Network, 2014). Our tomographic 3-D model will be available in the IRIS EMC - Reference Earth Models repository (http://ds.iris.edu/ds/products/emc-earthmodels/).

Acknowledgments

This study was partially funded by the SEISCOPE consortium (http://seiscope2.osug.fr), sponsored by AKERBP, CGG, EXXON-MOBIL, GEOLINKS, JGI, PETROBRAS, SHELL, SINOPEC, and TOTALENERGIES, and by the RGF program (Référentiel Géologique de la France, (http://rgf.brgm.fr/). It is part of the AlpArray-FR project funded by Agence Nationale de la Recherche (contract ANR-15-CE31-0015) and by Labex OSUG@2020 (Investissements d'Avenir, ANR-10-LABX-56). The deployment of OBSs for 8 months in the Liguro-Provençal basin was funded by project AlpArray-FR for the French component, and by the LOBSTER project that is part of the German Priority Programme SPP2017 4D-MB for the German component. This study was granted access to the HPC resources of the Dahu platform of the CIMENT infrastructure (https://gricad.univ-grenoble-alpes.fr/), which is supported by the Auvergne-Rhône-Alpes region (grant CPER07-13CIRA), the Labex OSUG@2020 (reference ANR10 LABX56) and the Equip@Meso project (reference ANR-10-EQPX-29-01) of the program 'Investissements d'Avenir' supervised by the Agence Nationale de la Recherche and the HPC resources of IDRIS/TGCC under allocation 046091 by GENCI. We are grateful to the editor and two anonymous reviewers whose comments improved our manuscript. We warmly thank Jean Virieux for computing and providing the first-arrival traveltime data. We thank Yang Lu for his constructive feedback on our inversion methodology. We thank Aya Cheaib, Dorian Bienveignant and Stephane Schwartz for their help in setting up the geological map. We are grateful to the operators of European permanent seismic networks who make their data available through EIDA (http://www.orfeus-eu.org/data/eida/). We are grateful to the captains and crews of R.V. Pourquoi Pas?

(France) and R.V. Maria S. Merian (Germany) for their work during the AlpArray-Leg-1 deployment cruise (doi:10.17600/17000400) and the MSM71-LOBSTER recovery cruise (doi:10.3289/GEOMAR_REP_NS_41_2018). We also thank all members of the scientific crews, in particular C. Aubert, S. Besançon and R. Daniel. The DEPAS pool provided 16 sea-bottom instruments used in his work, while the INSU-IPGP pool provided 7 broadband OBSs.

Appendix A

CIFALPS Team

Coralie Aubert, Elena Eva, Stéphane Guillot, Marco G. Malusa, Silvia Pondrelli, Simone Salimbeni, Stefano Solarino, Liang Zhao.

AlpArray Working Group

György Hetényi, Rafael Abreu, Ivo Allegretti, Maria-Theresia Apoloner, Coralie Aubert, Simon Besançon, Maxime Bès de Berc, Götz Bokelmann, Didier Brunel, Marco Capello, Martina Čarman, Adriano Cavaliere, Jérôme Chèze, Claudio Chiarabba, John Clinton, Glenn Cougoulat, Wayne C. Crawford, Luigia Cristiano, Tibor Czifra, Ezio D'Alema, Stefania Danesi, Romuald Daniel, Anke Dannowski, Iva Dasović, Anne Deschamps, Jean-Xavier Dessa, Cécile Doubre, Sven Egdorf, ETHZ-SED Electronics Lab, Tomislav Fiket, Kasper Fischer, Wolfgang Friederich, Florian Fuchs, Sigward Funke, Domenico Giardini, Aladino Govoni, Zoltán Gráczer, Gidera Gröschl, Stefan Heimers, Ben Heit, Davorka Herak, Marijan Herak, Johann Huber, Dejan Jaríc, Petr Jedlička, Yan Jia, Hélène Jund, Edi Kissling, Stefan Klingen, Bernhard Klotz, Petr Kolínský, Heidrun Kopp, Michael Korn, Josef Kotek, Lothar Kühne, Krešo Kuk, Dietrich Lange, Jürgen Loos, Sara Lovati, Deny Malen- gros, Lucia Margheriti, Christophe Maron, Xavier Martin, Marco Massa, Francesco Mazzarini, Thomas Meier, Laurent Métral, Irene Molinari, Milena Moretti, Anna Nardi, Jurij Pahor, Anne Paul, Catherine Péque- gnat, Daniel Petersen, Damiano Pesaresi, Davide Piccinini, Claudia Piromallo, Thomas Plenefisch, Jaroslava Plomerová, Silvia Pondrelli, Snježan Prevolnik, Roman Racine, Marc Régnier, Miriam Reiss, Joachim Ritter, Georg Rümpker, Simone Salimbeni, Marco Santulin, Werner Scherer, Sven Schippkus, Detlef Schulte-Kortnack, Vesna Šipka, Stefano Solarino, Daniele Spallarossa, Kathrin Spieker, Josip Stipčević, Angelo Strollo, Bálint Süle, Gyöngyvér Szanyi, Eszter Szűcs, Christine Thomas, Martin Thorwart, Frederik Tilmann, Stefan Ueding, Massimiliano Vallocchia, Luděk Vecsey, René Voigt, Joachim

Wassermann, Zoltán Wéber, Christian Weidle, Viktor Wesztergom, Gauthier Weyland, Stefan Wiemer, Felix Wolf, David Wolyniec, Thomas Zieke, Mladen Živčić, Helena Žlebčíková.

References

AlpArray Seismic Network. (2014). *Eastern Alpine Seismic Investigation (EASI) - AlpArray Complimentary Experiment [Dataset].* AlpArray Working Group. doi: https://doi.org/10.12686/alparray/xt_2014

AlpArray Seismic Network. (2015). *AlpArray Seismic Network (AASN) temporary component [Dataset].* AlpArray Working Group. doi: 10.12686/ALPARRAY/Z3_2015

Beller, S., Monteiller, V., Operto, S., Nolet, G., Paul, A., & Zhao, L. (2018, 02). Lithospheric architecture of the South-Western Alps revealed by multiparameter teleseismic full-waveform inversion. *Geophysical Journal International*, *212*, 1369-1388. doi: 10.1093/gji/ggx216

Bensen, G., Ritzwoller, M., Barmin, M., Levshin, A. L., Lin, F., Moschetti, M., ... Yang, Y. (2007). Processing seismic ambient noise data to obtain reliable broad-band surface wave dispersion measurements. *Geophysical journal international*, *169*(3), 1239–1260.

Brocher, T. (2005, 12). Empirical Relations between Elastic Wavespeeds and Density in the Earth's Crust. *Bulletin of the Seismological Society of America*, *95*, 2081-2092. doi: 10.1785/0120050077

Campillo, M. (2006). Phase and correlation in 'random' seismic fields and the reconstruction of the green function. *Pure and applied geophysics*, *163*, 475–502.

Cao, J., Brossier, R., Górszczyk, A., Métivier, L., & Virieux, J. (2022). 3-d multiparameter full-waveform inversion for ocean-bottom seismic data using an efficient fluid–solid coupled spectral-element solver. *Geophysical Journal International*, *229*(1), 671–703.

Carvalho, J., Silveira, G., Kiselev, S., Custódio, S., Ramalho, R. S., Stutzmann, E., & Schimmel, M. (2022, 07). Crustal and uppermost mantle structure of Cape Verde from ambient noise tomography. *Geophysical Journal International*, *231*(2), 1421-1433. Retrieved from `https://doi.org/10.1093/gji/ggac254` doi: 10.1093/gji/ggac254

Cerveny, V. (2003). *Seismic ray theory.* Acoustical Society of America.

Chen, M., Huang, H., Yao, H., van der Hilst, R., & Niu, F. (2014). Low wave speed zones in the crust beneath se tibet revealed by ambient noise adjoint tomography. *Geophysical Research Letters*, *41*(2), 334–340.

Chopin, C. (1984, May). Coesite and pure pyrope in high-grade blueschists of the West-

ern Alps: a first record and some consequences. *Contributions to Mineralogy and Petrology*, *86*(2), 107-118. doi: 10.1007/BF00381838

Contrucci, I., Nercessian, A., Béthoux, N., Mauffret, A., & Pascal, G. (2001). A ligurian (western mediterranean sea) geophysical transect revisited. *Geophysical Journal International*, *146*(1), 74–97.

Dannowski, A., Kopp, H., Grevemeyer, I., Lange, D., Thorwart, M., Bialas, J., & Wollatz-Vogt, M. (2020). Seismic evidence for failed rifting in the ligurian basin, western alpine domain. *Solid Earth*, *11*(3), 873–887. Retrieved from `https://se.copernicus.org/articles/11/873/2020/` doi: 10.5194/se-11-873-2020

Delaney, E., Ermert, L., Sager, K., Kritski, A., Bussat, S., & Fichtner, A. (2017). Passive seismic monitoring with nonstationary noise sourcesmonitoring with nonstationary noise. *Geophysics*, *82*(4), KS57–KS70.

Diehl, T., Husen, S., Kissling, E., & Deichmann, N. (2009, 11). High-resolution 3-D P-wave model of the Alpine crust. *Geophysical Journal International*, *179*(2), 1133-1147. Retrieved from `https://doi.org/10.1111/j.1365-246X.2009.04331.x` doi: 10.1111/j.1365-246X.2009.04331.x

Di Stefano, R., Kissling, E., Chiarabba, C., Amato, A., & Giardini, D. (2009). Shallow subduction beneath italy: Three-dimensional images of the adriatic-european-tyrrhenian lithosphere system based on high-quality p wave arrival times. *Journal of Geophysical Research: Solid Earth*, *114*(B5).

Duchêne, S., Blichert-Toft, J., Luais, B., Télouk, P., Lardeaux, J.-M., & Albarede, F. (1997). The Lu–Hf dating of garnets and the ages of the alpine high-pressure metamorphism. *Nature*, *387*(6633), 586–589.

Dumont, T., Schwartz, S., Guillot, S., Simon-Labric, T., Tricart, P., & Jourdan, S. (2012). Structural and sedimentary records of the oligocene revolution in the western alpine arc. *Journal of Geodynamics*, *56*, 18–38.

Eddy, C. L., & Ekström, G. (2014). Local amplification of rayleigh waves in the continental united states observed on the usarray. *Earth and Planetary Science Letters*, *402*, 50–57.

Ermert, L., Sager, K., Afanasiev, M., Boehm, C., & Fichtner, A. (2017). Ambient seismic source inversion in a heterogeneous earth: Theory and application to the earth's hum. *Journal of Geophysical Research: Solid Earth*, *122*(11), 9184–9207.

Ermert, L., Sager, K., Nissen-Meyer, T., & Fichtner, A. (2021). Multifrequency inversion

of global ambient seismic sources. *Geophysical Journal International*, *225*(3), 1616–1623.

Ermert, L., Villasenor, A., & Fichtner, A. (2016). Cross-correlation imaging of ambient noise sources. *Geophysical Journal International*, *204*(1), 347–364.

Faccenna, C., Becker, T. W., Auer, L., Billi, A., Boschi, L., Brun, J. P., ... Serpelloni, E. (2014). Mantle dynamics in the mediterranean. *Reviews of Geophysics*, *52*(3), 283-332. Retrieved from `https://agupubs.onlinelibrary.wiley.com/doi/abs/10.1002/2013RG000444` doi: https://doi.org/10.1002/2013RG000444

Federal Institute for Geosciences, & Natural Resources (BGR). (1976). German Regional Seismic Network (GRSN) [Dataset]. Retrieved 2020-08-20, from `https://www.seismologie.bgr.de/doi/grsn/` (Publisher: Federal Institute for Geosciences and Natural Resources (BGR)) doi: 10.25928/MBX6-HR74

Fichtner, A. (2014). Source and processing effects on noise correlations. *Geophysical Journal International*, *197*(3), 1527–1531.

Fichtner, A., Bowden, D., & Ermert, L. (2020). Optimal processing for seismic noise correlations. *Geophysical Journal International*, *223*(3), 1548–1564.

Fichtner, A., Stehly, L., Ermert, L., & Boehm, C. (2016). Generalised interferometry-i. theory for inter-station correlations. *Geophysical Journal International*, ggw420.

Fichtner, A., & Villaseñor, A. (2015). Crust and upper mantle of the western mediterranean–constraints from full-waveform inversion. *Earth and Planetary Science Letters*, *428*, 52–62.

Froment, B., Campillo, M., Roux, P., Gouedard, P., Verdel, A., & Weaver, R. L. (2010). Estimation of the effect of nonisotropically distributed energy on the apparent arrival time in correlations. *Geophysics*, *75*(5), SA85–SA93.

GEOFON Data Centre. (1993). GEOFON seismic network [dataset]. Retrieved 2020-08-20, from `http://geofon.gfz-potsdam.de/doi/network/GE` (Publisher: Deutsches GeoForschungsZentrum GFZ) doi: 10.14470/TR560404

Gueguen, E., Doglioni, C., & Fernandez, M. (1998). On the post-25 ma geodynamic evolution of the western mediterranean. *Tectonophysics*, *298*(1), 259-269. Retrieved from `https://www.sciencedirect.com/science/article/pii/S0040195198001899` doi: https://doi.org/10.1016/S0040-1951(98)00189-9

Guerin, G., Rivet, D., Deschamps, A., Larroque, C., Mordret, A., Dessa, J.-X., & Martin, X. (2020). High resolution ambient noise tomography of the southwestern alps and

the ligurian margin. *Geophysical Journal International*, *220*(2), 806–820.

Guillot, S., Hattori, K., Agard, P., Schwartz, S., & Vidal, O. (2009). Exhumation Processes in Oceanic and Continental Subduction Contexts: A Review. In S. Lallemand & F. Funiciello (Eds.), *Subduction zone geodynamics* (pp. 175–205). Berlin, Heidelberg: Springer Berlin Heidelberg.

Hanasoge, S. M. (2014). Measurements and kernels for source-structure inversions in noise tomography. *Geophysical Journal International*, *196*(2), 971–985.

Handy, M. R., Schmid, S. M., Bousquet, R., Kissling, E., & Bernoulli, D. (2010). Reconciling plate-tectonic reconstructions of alpine tethys with the geological–geophysical record of spreading and subduction in the alps. *Earth-Science Reviews*, *102*(3-4), 121–158.

Hetényi, G., Molinari, I., & Clinton, J. (2018, 09). The AlpArray Seismic Network: A Large-Scale European Experiment to Image the Alpine Orogen. *Surveys in Geophysics*, *39*. doi: 10.1007/s10712-018-9472-4

Igel, J. K., Bowden, D. C., & Fichtner, A. (2023). Sans: Publicly available daily multi-scale seismic ambient noise source maps. *Journal of Geophysical Research: Solid Earth*, *128*(1), e2022JB025114.

Igel, J. K., Ermert, L. A., & Fichtner, A. (2021). Rapid finite-frequency microseismic noise source inversion at regional to global scales. *Geophysical Journal International*, *227*(1), 169–183.

INGV Seismological Data Centre. (2006). Rete Sismica Nazionale (RSN) [Dataset]. Retrieved 2020-08-20, from `http://cnt.rm.ingv.it/instruments/network/IV` (Publisher: Istituto Nazionale di Geofisica e Vulcanologia (INGV), Italy) doi: 10.13127/SD/X0FXNH7QFY

Institut Cartogràfic I Geològic De Catalunya - Institut D'Estudis Catalans. (1984). *Catalan Seismic Network [Dataset].* Retrieved 2019-02-08, from `http://www.fdsn.org/doi/10.7914/SN/CA` (Publisher: International Federation of Digital Seismograph Networks) doi: 10.7914/SN/CA

Institut de Physique du Globe de Paris (IPGP), & Ecole et Observatoire des Sciences de la Terre de Strasbourg (EOST). (1982). *GEOSCOPE, French Global Network of broad band seismic stations [Dataset].* Institut de Physique du Globe de Paris (IPGP). Retrieved 2019-02-08, from `http://geoscope.ipgp.fr/networks/detail/G/` (Publisher: Institut de Physique du Globe de Paris (IPGP)) doi: 10.18715/GEOSCOPE.G

Institute Of Geophysics Of The Academy Of Sciences Of The Czech Republic. (1973).

Czech Regional Seismic Network [Dataset]. Retrieved 2019-02-08, from http://www.fdsn.org/doi/10.7914/SN/CZ (Publisher: International Federation of Digital Seismograph Networks) doi: 10.7914/SN/CZ

Instituto Geografico Nacional, Spain. (1999). *Spanish Digital Seismic Network [Dataset].* International Federation of Digital Seismograph Networks. Retrieved 2020-08-21, from http://www.fdsn.org/networks/detail/ES/ (Publisher: International Federation of Digital Seismograph Networks) doi: 10.7914/SN/ES

Jolivet, L., & Faccenna, C. (2000). Mediterranean extension and the africa-eurasia collision. *Tectonics*, *19*(6), 1095–1106.

Jolivet, L., Romagny, A., Gorini, C., Maillard, A., Thinon, I., Couëffé, R., ... Séranne, M. (2020). Fast dismantling of a mountain belt by mantle flow: Late-orogenic evolution of pyrenees and liguro-provençal rifting. *Tectonophysics*, *776*, 228312. Retrieved from https://www.sciencedirect.com/science/article/pii/S0040195119304275 doi: https://doi.org/10.1016/j.tecto.2019.228312

Kimman, W., & Trampert, J. (2010). Approximations in seismic interferometry and their effects on surface waves. *Geophysical Journal International*, *182*(1), 461–476.

KNMI. (1993). *Netherlands Seismic and Acoustic Network [Dataset].* Retrieved 2019-02-08, from http://rdsa.knmi.nl/network/NL/ (Publisher: Royal Netherlands Meteorological Institute (KNMI)) doi: 10.21944/e970fd34-23b9-3411-b366-e4f72877d2c5

Komatitsch, D., & Tromp, J. (1999). Introduction to the spectral element method for three-dimensional seismic wave propagation. *Geophysical journal international*, *139*(3), 806–822.

Komatitsch, D., & Tromp, J. (2002). Spectral-element simulations of global seismic wave propagation—i. validation. *Geophysical Journal International*, *149*(2), 390–412.

Kvapil, J., Plomerová, J., Kampfová Exnerová, H., Babuška, V., Hetényi, G., & Group, A. W. (2021). Transversely isotropic lower crust of variscan central europe imaged by ambient noise tomography of the bohemian massif. *Solid Earth*, *12*(5), 1051–1074. Retrieved from https://se.copernicus.org/articles/12/1051/2021/ doi: 10.5194/se-12-1051-2021

Kästle, E. D., El-Sharkawy, A., Boschi, L., Meier, T., Rosenberg, C., Bellahsen, N., ... Weidle, C. (2018). Surface Wave Tomography of the Alps Using Ambient-Noise and Earthquake Phase Velocity Measurements. *Journal of Geophysical Research: Solid Earth*, *123*(2), 1770-1792. Retrieved from https://agupubs.onlinelibrary.wiley.com/

doi/abs/10.1002/2017JB014698 doi: https://doi.org/10.1002/2017JB014698

Liu, Y., Niu, F., Chen, M., & Yang, W. (2017). 3-d crustal and uppermost mantle structure beneath ne china revealed by ambient noise adjoint tomography. *Earth and Planetary Science Letters*, *461*, 20–29.

Lobkis, O. I., & Weaver, R. L. (2001). On the emergence of the green's function in the correlations of a diffuse field. *The Journal of the Acoustical Society of America*, *110*(6), 3011-3017. Retrieved from https://doi.org/10.1121/1.1417528 doi: 10.1121/1.1417528

Lomax, A., Virieux, J., Volant, P., & Berge-Thierry, C. (2000). Probabilistic earthquake location in 3d and layered models: Introduction of a metropolis-gibbs method and comparison with linear locations. *Advances in seismic event location*, 101–134.

Lombardi, D., Braunmiller, J., Kissling, E., & Giardini, D. (2008). Moho depth and poisson's ratio in the western-central alps from receiver functions. *Geophysical Journal International*, *173*(1), 249–264.

Lu, Y., Stehly, L., Brossier, R., Paul, A., & AlpArray Working Group. (2020, 03). Imaging Alpine crust using ambient noise wave-equation tomography. *Geophysical Journal International*, *222*(1), 69-85. Retrieved from https://doi.org/10.1093/gji/ggaa145 doi: 10.1093/gji/ggaa145

Lu, Y., Stehly, L., Paul, A., & AlpArray Working Group. (2018, 05). High-resolution surface wave tomography of the European crust and uppermost mantle from ambient seismic noise. *Geophysical Journal International*, *214*(2), 1136-1150. Retrieved from https://doi.org/10.1093/gji/ggy188 doi: 10.1093/gji/ggy188

Luo, Y., & Schuster, G. T. (1991). Wave-equation traveltime inversion. *Geophysics*, *56*(5), 645–653.

Magrini, F., Diaferia, G., El-Sharkawy, A., Cammarano, F., van der Meijde, M., Meier, T., & Boschi, L. (2022). Surface-wave tomography of the central-western mediterranean: New insights into the liguro-provençal and tyrrhenian basins. *Journal of Geophysical Research: Solid Earth*, *127*(3), e2021JB023267.

Makris, J., Egloff, F., Nicolich, R., & Rihm, R. (1999). Crustal structure from the ligurian sea to the northern apennines—a wide angle seismic transect. *Tectonophysics*, *301*(3-4), 305–319.

Malusà, M. G., Guillot, S., Zhao, L., Paul, A., Solarino, S., Dumont, T., ... Yuan, H. (2021). The deep structure of the alps based on the cifalps seis-

mic experiment: A synthesis. *Geochemistry, Geophysics, Geosystems*, *22*(3), e2020GC009466. Retrieved from https://agupubs.onlinelibrary.wiley.com/doi/abs/10.1029/2020GC009466 (e2020GC009466 2020GC009466) doi: https://doi.org/10.1029/2020GC009466

Métivier, L., & Brossier, R. (2016). The seiscope optimization toolbox: A large-scale nonlinear optimization library based on reverse communication. *Geophysics*, *81*(2), F1–F15.

Molinari, I., & Morelli, A. (2011). Epcrust: a reference crustal model for the european plate. *Geophysical Journal International*, *185*(1), 352–364.

Mordret, A., Landès, M., Shapiro, N., Singh, S., & Roux, P. (2014). Ambient noise surface wave tomography to determine the shallow shear velocity structure at valhall: depth inversion with a neighbourhood algorithm. *Geophysical Journal International*, *198*(3), 1514–1525.

Nayfeh, A. H. (1995). *Wave propagation in layered anisotropic media: With application to composites*. Elsevier.

Nicolas, A., Hirn, A., Nicolich, R., & Polino, R. (1990, 07). Lithospheric wedging in the western Alps inferred from the ECORS-CROP traverse. *Geology*, *18*(7), 587-590. Retrieved from https://doi.org/10.1130/0091-7613(1990)018<0587:LWITWA>2.3.CO;2 doi: 10.1130/0091-7613(1990)018⟨0587:LWITWA⟩2.3.CO;2

Nocedal, J. (1980). Updating quasi-newton matrices with limited storage. *Mathematics of computation*, *35*(151), 773–782.

Nouibat, A., Stehly, L., Paul, A., Schwartz, S., Bodin, T., Dumont, T., ... Group, A. W. (2022a). Lithospheric transdimensional ambient-noise tomography of w-europe: implications for crustal-scale geometry of the w-alps. *Geophysical Journal International*, *229*(2), 862–879.

Nouibat, A., Stehly, L., Paul, A., Schwartz, S., Rolland, Y., Dumont, T., ... Group, A. W. (2022b). Ambient-noise tomography of the ligurian-provence basin using the alparray onshore-offshore network: Insights for the oceanic domain structure. *Journal of Geophysical Research: Solid Earth*, *127*(8), e2022JB024228.

Paul, A., Malusà, M. G., Solarino, S., Salimbeni, S., Eva, E., Nouibat, A., ... Zhao, L. (2022). Along-strike variations in the fossil subduction zone of the western alps revealed by the cifalps seismic experiments and their implications for exhumation of (ultra-) high-pressure rocks. *Earth and Planetary Science Letters*, *598*,

117843. Retrieved from https://www.sciencedirect.com/science/article/pii/S0012821X22004794 doi: https://doi.org/10.1016/j.epsl.2022.117843

Petersen, G. M., Cesca, S., Heimann, S., Niemz, P., Dahm, T., Kühn, D., ... working groups, A.-S.-D. (2021). Regional centroid moment tensor inversion of small to moderate earthquakes in the alps using the dense alparray seismic network: challenges and seismotectonic insights. *Solid Earth*, *12*(6), 1233–1257. Retrieved from https://se.copernicus.org/articles/12/1233/2021/ doi: 10.5194/se-12-1233-2021

Piana Agostinetti, N., & Amato, A. (2009). Moho depth and vp/vs ratio in peninsular italy from teleseismic receiver functions. *Journal of Geophysical Research: Solid Earth*, *114*(B6).

Plessix, R.-E. (2006). A review of the adjoint-state method for computing the gradient of a functional with geophysical applications. *Geophysical Journal International*, *167*(2), 495–503.

Podvin, P., & Lecomte, I. (1991). Finite difference computation of traveltimes in very contrasted velocity models: a massively parallel approach and its associated tools. *Geophysical Journal International*, *105*(1), 271-284. Retrieved from https://onlinelibrary.wiley.com/doi/abs/10.1111/j.1365-246X.1991.tb03461.x doi: https://doi.org/10.1111/j.1365-246X.1991.tb03461.x

Polino, R., Dal Piaz, G. V., & Gosso, G. (1990). Tectonic erosion at the adria margin and accretionary processes for the cretaceous orogeny of the alps. *Mémoires de la Société géologique de France (1833)*, *156*, 345–367.

Potin, B. (2016). *Les alpes occidentales: tomographie, localisation de séismes et topographie du moho*. Université Grenoble Alpes.

Qiao, L., Yao, H., Lai, Y.-C., Huang, B.-S., & Zhang, P. (2018). Crustal structure of southwest china and northern vietnam from ambient noise tomography: Implication for the large-scale material transport model in se tibet. *Tectonics*, *37*(5), 1492–1506.

RESIF. (1995). *RESIF-RLBP French Broad-band network, RESIF-RAP strong motion network and other seismic stations in metropolitan France [Dataset]*. Retrieved 2019-02-08, from http://seismology.resif.fr/#NetworkConsultPlace:FR (Publisher: RESIF - Réseau Sismologique et géodésique Français) doi: 10.15778/resif.fr

Rollet, N., Déverchère, J., Beslier, M.-O., Guennoc, P., Réhault, J.-P., Sosson, M., & Truffert, C. (2002). Back arc extension, tectonic inheritance, and volcanism in the ligurian sea, western mediterranean. *Tectonics*, *21*(3), 6-1-

6-23. Retrieved from https://agupubs.onlinelibrary.wiley.com/doi/abs/10.1029/2001TC900027 doi: https://doi.org/10.1029/2001TC900027

Roux, P., Sabra, K. G., Gerstoft, P., Kuperman, W., & Fehler, M. C. (2005). P-waves from cross-correlation of seismic noise. *Geophysical Research Letters*, *32*(19).

Royal Observatory Of Belgium. (1985). *Belgian Seismic Network [Dataset].* Retrieved 2019-02-08, from http://www.fdsn.org/doi/10.7914/SN/BE (Publisher: International Federation of Digital Seismograph Networks) doi: 10.7914/SN/BE

Sadeghi-Bagherabadi, A., Vuan, A., Aoudia, A., Parolai, S., T. A., Group, A.-S.-D. W., ... Tilmann, F. (2021). High-resolution crustal s-wave velocity model and moho geometry beneath the southeastern alps: New insights from the swath-d experiment. *Frontiers in Earth Science*, *9*, 188. Retrieved from https://www.frontiersin.org/article/10.3389/feart.2021.641113 doi: 10.3389/feart.2021.641113

Sager, K., Boehm, C., Ermert, L., Krischer, L., & Fichtner, A. (2018b). Sensitivity of seismic noise correlation functions to global noise sources. *Journal of Geophysical Research: Solid Earth*, *123*(8), 6911–6921.

Sager, K., Ermert, L., Boehm, C., & Fichtner, A. (2018a). Towards full waveform ambient noise inversion. *Geophysical Journal International*, *212*(1), 566–590.

Schippkus, S., Zigone, D., & Bokelmann, G. (2020). Azimuthal anisotropy in the wider vienna basin region: a proxy for the present-day stress field and deformation. *Geophysical Journal International*, *220*(3), 2056–2067.

Schmid, S. M., Fügenschuh, B., Kissling, E., & Schuster, R. (2004). Tectonic map and overall architecture of the alpine orogen. *Eclogae Geologicae Helvetiae*, *97*(1), 93–117.

Séranne, M. (1999). The gulf of lion continental margin (nw mediterranean) revisited by ibs: an overview. *Geological Society, London, Special Publications*, *156*(1), 15–36. Retrieved from https://sp.lyellcollection.org/content/156/1/15 doi: 10.1144/GSL.SP.1999.156.01.03

Slovenian Environment Agency. (2001). Seismic Network of the Republic of Slovenia [Dataset]. Retrieved 2020-08-21, from http://www.fdsn.org/doi/10.7914/SN/SL (Publisher: International Federation of Digital Seismograph Networks) doi: 10.7914/SN/SL

Snieder, R. (1986). 3-d linearized scattering of surface waves and a formalism for surface wave holography. *Geophysical Journal International*, *84*(3), 581–605.

Snieder, R. (2004). Extracting the green's function from the correlation of coda waves: A

derivation based on stationary phase. *Physical Review E*, *69*(4), 046610.

Snieder, R., Wapenaar, K., & Wegler, U. (2007). Unified green's function retrieval by cross-correlation; connection with energy principles. *Physical Review E*, *75*(3), 036103.

SNSN. (1904). *Swedish National Seismic Network [Dataset].* Retrieved 2019-02-08, from `http://www.snsn.se/network/` (Publisher: Uppsala University, Uppsala, Sweden) doi: 10.18159/SNSN

Spada, M., Bianchi, I., Kissling, E., Agostinetti, N. P., & Wiemer, S. (2013, 05). Combining controlled-source seismology and receiver function information to derive 3-D Moho topography for Italy. *Geophysical Journal International*, *194*(2), 1050-1068. Retrieved from `https://doi.org/10.1093/gji/ggt148` doi: 10.1093/gji/ggt148

Stehly, L., & Boué, P. (2017). On the interpretation of the amplitude decay of noise correlations computed along a line of receivers. *Geophysical Journal International*, *209*(1), 358–372.

Swiss Seismological Service (SED) At ETH Zurich. (1983). National Seismic Networks of Switzerland [Dataset]. Retrieved 2020-08-20, from `http://networks.seismo.ethz.ch/networks/ch/` (Publisher: ETH Zürich) doi: 10.12686/SED/NETWORKS/CH

Tape, C., Liu, Q., Maggi, A., & Tromp, J. (2010). Seismic tomography of the southern california crust based on spectral-element and adjoint methods. *Geophysical Journal International*, *180*(1), 433–462.

Trinh, P.-T., Brossier, R., Métivier, L., Tavard, L., & Virieux, J. (2019). Efficient time-domain 3d elastic and viscoelastic full-waveform inversion using a spectral-element method on flexible cartesian-based mesh. *Geophysics*, *84*(1), R75–R97.

Trinh, P.-T., Brossier, R., Métivier, L., Virieux, J., & Wellington, P. (2017). Bessel smoothing filter for spectral-element mesh. *Geophysical Journal International*, *209*(3), 1489–1512.

Tromp, J., Luo, Y., Hanasoge, S., & Peter, D. (2010). Noise cross-correlation sensitivity kernels. *Geophysical Journal International*, *183*(2), 791–819.

Tromp, J., Tape, C., & Liu, Q. (2005). Seismic tomography, adjoint methods, time reversal and banana-doughnut kernels. *Geophysical Journal International*, *160*(1), 195–216.

Tsai, V. C. (2009). On establishing the accuracy of noise tomography travel-time measurements in a realistic medium. *Geophysical Journal International*, *178*(3), 1555–1564.

Tsai, V. C. (2011). Understanding the amplitudes of noise correlation measurements. *Journal of Geophysical Research: Solid Earth*, *116*(B9).

University Of Zagreb. (2001). *Croatian Seismograph Network [Dataset].* Retrieved 2020-08-20, from `http://www.fdsn.org/networks/detail/CR/` (Publisher: International Federation of Digital Seismograph Networks) doi: 10.7914/SN/CR

Virieux, J., & Operto, S. (2009). An overview of full-waveform inversion in exploration geophysics. *Geophysics*, *74*(6), WCC1–WCC26.

Virieux, J., Paul, A., Langlais, M., Janex, G., Gueguen, P., Helmstetter, A., & Stehly, L. (2023). Assessing the reliability of local earthquake tomography for crustal imaging: 30 years of records in the Western Alps as a case study. *Geophysical Journal International*, *In review*.

Waldhauser, F., Kissling, E., Ansorge, J., & Mueller, S. (1998). Three dimensional interface modelling with two-dimensional seismic data: the alpine crust-mantle boundary. *Geophysical Journal International*, *135*(1), 264–278.

Wapenaar, K. (2004, Dec). Retrieving the elastodynamic green's function of an arbitrary inhomogeneous medium by cross correlation. *Phys. Rev. Lett.*, *93*, 254301. Retrieved from `https://link.aps.org/doi/10.1103/PhysRevLett.93.254301` doi: 10.1103/PhysRevLett.93.254301

Warner, M., Ratcliffe, A., Nangoo, T., Morgan, J., Umpleby, A., Shah, N., ... others (2013). Anisotropic 3d full-waveform inversion. *Geophysics*, *78*(2), R59–R80.

Weaver, R. L. (2005). Information from seismic noise. *Science*, *307*, 1568 - 1569.

Weaver, R. L., & Lobkis, O. I. (2001). Ultrasonics without a source: Thermal fluctuation correlations at mhz frequencies. *Physical Review Letters*, *87*(13), 134301.

Wolf, F. N., Lange, D., Dannowski, A., Thorwart, M., Crawford, W., Wiesenberg, L., ... the AlpArray Working Group (2021). 3D crustal structure of the Ligurian Basin revealed by surface wave tomography using ocean bottom seismometer data. *Solid Earth*, *12*(11), 2597–2613. Retrieved from `https://se.copernicus.org/articles/12/2597/2021/` doi: 10.5194/se-12-2597-2021

Yang, Y., & Ritzwoller, M. H. (2008). Characteristics of ambient seismic noise as a source for surface wave tomography. *Geochemistry, Geophysics, Geosystems*, *9*(2).

Yuan, H., French, S., Cupillard, P., & Romanowicz, B. (2014). Lithospheric expression of geological units in central and eastern north america from full waveform tomography. *Earth and Planetary Science Letters*, *402*, 176–186.

ZAMG-Zentralanstalt Für Meterologie Und Geodynamik. (1987). Austrian Seismic Network [Dataset]. Retrieved 2020-08-20, from `http://www.fdsn.org/doi/10.7914/SN/OE`

(Publisher: International Federation of Digital Seismograph Networks) doi: 10.7914/SN/OE

Zhao, L., Malusà, M. G., Yuan, H., Paul, A., Guillot, S., Lu, Y., ... Bodin, T. (2020, May). Evidence for a serpentinized plate interface favouring continental subduction. *Nature Communications*, *11*, 2171. Retrieved from `https://hal.archives-ouvertes.fr/hal-02560510` doi: 10.1038/s41467-020-15904-7

Zhao, L., Paul, A., Guillot, S., Solarino, S., Malusà, M., Zheng, T., ... Wang, Q. (2015, 09). First Seismic Evidence for Continental Subduction beneath the Western Alps. *Geology*, *43*, 815-818. doi: 10.1130/G36833.1

Zhao, L., Paul, A., Solarino, S., & RESIF. (2018). *Seismic network XT: CIFALPS temporary experiment (China-Italy-France Alps seismic transect) [Dataset].* RESIF - Réseau Sismologique et géodésique Français. doi: 10.15778/RESIF.XT2018

Zheng, Y., Fang, X., Liu, J., & Fehler, M. C. (2013). Scholte waves generated by seafloor topography. *arXiv preprint arXiv:1306.4383*.

Zhu, H., Bozdağ, E., Peter, D., & Tromp, J. (2012). Structure of the european upper mantle revealed by adjoint tomography. *Nature Geoscience*, *5*(7), 493–498.

Zhu, J., Popovics, J. S., & Schubert, F. (2004). Leaky rayleigh and scholte waves at the fluid–solid interface subjected to transient point loading. *The Journal of the Acoustical Society of America*, *116*(4), 2101–2110.